ARTICLE

PD-1 and BTLA regulate T cell signaling differentially and only partially through SHP1 and SHP2

Xiaozheng Xu[1]*, Bowen Hou[2]*, Amitkumar Fulzele[1], Takeya Masubuchi[1], Yunlong Zhao[1], Zijun Wu[1], Yanyan Hu[2], Yong Jiang[3], Yanzhe Ma[1], Haopeng Wang[3], Eric J. Bennett[1], Guo Fu[2], and Enfu Hui[1]

Blockade antibodies of the immunoinhibitory receptor PD-1 can stimulate the anti-tumor activity of T cells, but clinical benefit is limited to a fraction of patients. Evidence suggests that BTLA, a receptor structurally related to PD-1, may contribute to resistance to PD-1 targeted therapy, but how BTLA and PD-1 differ in their mechanisms is debated. Here, we compared the abilities of BTLA and PD-1 to recruit effector molecules and to regulate T cell signaling. While PD-1 selectively recruited SHP2 over the stronger phosphatase SHP1, BTLA preferentially recruited SHP1 to more efficiently suppress T cell signaling. Contrary to the dominant view that PD-1 and BTLA signal exclusively through SHP1/2, we found that in SHP1/2 double-deficient primary T cells, PD-1 and BTLA still potently inhibited cell proliferation and cytokine production, albeit more transiently than in wild type T cells. Thus, PD-1 and BTLA can suppress T cell signaling through a mechanism independent of both SHP1 and SHP2.

Introduction

T cell activation is governed by both antigen-specific signals from T cell receptor (TCR) and antigen-nonspecific signals through coreceptors. The relative strength of these signaling pathways—with some promoting T cell activation (costimulatory) and others repressing T cell activation (coinhibitory)—is critical in shaping the overall immune response (Chen and Flies, 2013; Schildberg et al., 2016).

Several coreceptors belong to the B7 family of the Ig superfamily. Among these, CD28 is a central costimulatory receptor that, upon binding to its ligands CD80 (B7-1) or CD86 (B7-2; Lenschow et al., 1996), delivers essential positive signals for full activation of naive T cells (Lanzavecchia et al., 1999) and for proliferation of virus- and tumor-specific T cells (Kamphorst et al., 2017). Programmed cell death protein 1 (PD-1) and B and T lymphocyte attenuator (BTLA) are evolutionally and structurally related coinhibitory receptors that attenuate T cell activation (Carreno and Collins, 2003; Freeman et al., 2000; Nishimura and Honjo, 2001; Riley, 2009; Watanabe et al., 2003), acting as "checkpoints" to prevent overreactive T cells (Fuertes Marraco et al., 2015). PD-1 has two known ligands in the B7 family: the broadly expressed programmed death-ligand 1 (PD-L1; Freeman et al., 2000; Taube et al., 2012) and the higher affinity, more restrictedly expressed PD-L2 (Cheng et al., 2013; Latchman et al., 2001). Notably, the best studied ligand for BTLA, herpes virus entry mediator (HVEM; Compaan et al., 2005; Gonzalez et al., 2005; Sedy et al., 2005), is a member of the TNF receptor family rather than the B7 family (Croft, 2003; Morel et al., 2000).

PD-1 is absent on naive T cells, induced upon TCR activation to restrain excessive T cell–mediated tissue damage, and declines to basal levels upon antigen clearance (Keir et al., 2008). In contrast, BTLA is abundant on naive T cells, but its expression also decreases during T cell development and differentiation, particularly in CD8^{+} T cells (Baitsch et al., 2012; Derré et al., 2010; Hurchla et al., 2005). Indeed, down-regulation of PD-1 is essential for optimal function of effector T cells. In cancer patients, constitutive up-regulation of PD-1 restricts the anti-tumor activity of T cells (Baitsch et al., 2011; Mellman et al., 2011; Pardoll, 2012; Pauken and Wherry, 2015; Sharma and Allison, 2015). PD-1 blockade antibodies have shown impressive clinical activities against several human cancers in a small subset of patients (Hamid et al., 2013; Herbst et al., 2014; Powles et al., 2014; Rizvi et al., 2015; Topalian et al., 2012). Evidence suggests that BTLA might contribute to the observed resistance to PD-1 inhibitors. In human melanoma patients, BTLA is persistently expressed in tumor-specific CD8^{+} T cells and inhibits the function of these cells (Derré et al., 2010). BTLA/PD-1

[1]Division of Biological Sciences, University of California San Diego, La Jolla, CA;   [2]School of Life Sciences, Xiamen University, Xiamen, Fujian, China;   [3]School of Life Science and Technology, ShanghaiTech University, Shanghai, China.

*X. Xu and B. Hou contributed equally to this paper;   Correspondence to Guo Fu: guofu@xmu.edu.cn;   Enfu Hui: enfuhui@ucsd.edu;   Z. Wu's present address is Center for Biophysics and Quantitative Biology, University of Illinois at Urbana-Champaign, Champaign, IL.

coexpression is required for the dysfunction of human hepatocellular carcinoma infiltrated CD4^{+} T cells (Zhao et al., 2016). In mouse models, PD-1 and BTLA co-blockade restores T cell functions and promotes tumor control more effectively than PD-1 mono-blockade (Ahrends et al., 2017; Fourcade et al., 2012).

Both PD-1 and BTLA consist of an Ig-like ectodomain, a single transmembrane domain (TMD), and an intracellular tail. The tail of PD-1 contains two tyrosines, Y223 and Y248, embedded in an immunoreceptor-tyrosine-inhibitory motif (ITIM) and an immunoreceptor-tyrosine-switch motif (ITSM), respectively. The tail of BTLA contains both an ITIM (surrounding Y257) and an ITSM (surrounding Y282), akin to PD-1, plus two additional tyrosines (Y226 and Y243) N terminal to the ITIM (Chemnitz et al., 2006) that reportedly recruit the adaptor protein GRB2 (Gavrieli and Murphy, 2006).

Engagement of PD-1 with either PD-L1 or PD-L2 triggers phosphorylation of both Y223 and Y248 and recruitment of the protein tyrosine phosphatase (PTPase) Src-homology-2 (SH2) domain-containing phosphatase (SHP)2 via its tandem SH2 (tSH2) domains (Chemnitz et al., 2004; Yokosuka et al., 2012). PD-1–associated SHP2 dephosphorylates costimulatory receptors CD28 and CD226 and, to a lesser extent, the CD3ζ subunit of TCR (Hui et al., 2017; Wang et al., 2018). However, a recent study showed that PD-1 blockade enhances tumor control in mice with a T cell–specific SHP2 deletion (Rota et al., 2018), casting doubt on classical models in which SHP2 is the key effector of PD-1 function. A role for the SHP2 paralog SHP1 in the PD-1 pathway would offer a resolution to this apparent conflict, but this contribution of SHP1 to PD-1 signaling remains contentious. While earlier studies observed no SHP1 recruitment to PD-1 (Okazaki et al., 2001; Sheppard et al., 2004), a more recent study suggests that SHP1 can fully support PD-1 function in a SHP2-deficient background (Celis-Gutierrez et al., 2019).

Less is known about BTLA signaling and how it differs mechanistically from that of PD-1. Co-immunoprecipitation (coIP) experiments in transfected cell lines suggest that HVEM:BTLA interaction elicits BTLA phosphorylation and recruitment of both SHP1 and SHP2 (Celis-Gutierrez et al., 2019; Gavrieli et al., 2003; Sedy et al., 2005). However, other studies reported that BTLA recruits SHP1 but not SHP2 in HVEM-stimulated primary CD4^{+} T cells (Chemnitz et al., 2006; Mintz et al., 2019). Hence, further studies are needed to define the BTLA signaling pathway.

In the present study, we compared BTLA and PD-1 signaling using biochemical reconstitution, engineered cell lines, and primary T cell cultures. We found that upon ligation, PD-1 recruited the weaker PTPase SHP2, but not the stronger PTPase SHP1 even in a SHP2 knockout (KO) background, whereas BTLA preferentially recruited SHP1. Moreover, SHP2, irrespective of recruitment by either PD-1 or BTLA, primarily dephosphorylated CD28 but not CD3ζ. In contrast, the BTLA:SHP1 complex potently dephosphorylated both CD28 and CD3ζ. Strikingly, in primary T cells lacking both SHP1 and SHP2, PD-1 and BTLA still suppressed T cell proliferation and cytokine production. These results revealed a functional disparity between PD-1 and BTLA, and the existence of SHP1/2–independent mechanisms for their inhibitory signaling.

Results

BTLA and PD-1 signaling inhibit interleukin 2 (IL-2) production from T cells

We first sought to establish a cell culture system to compare PD-1 and BTLA signaling in parallel. We used Jurkat T cells as the responder cells and Raji B cells as the antigen-presenting cells (APCs). Raji B cells preloaded with the superantigen staphylococcal enterotoxin E (SEE) stimulate TCR signaling in Jurkat T cells (Choi et al., 1989). Meanwhile, the Raji-Jurkat cell interaction also triggers CD28 costimulatory signaling due to the expression of B7 family ligand molecules on Raji cells (Tatsumi et al., 1997). Previous studies showed that the phosphorylation of intracellular tyrosine motifs is required for both PD-1 and BTLA functions. Therefore, we used tyrosine mutated PD-1 and BTLA as references to quantify the magnitude of inhibitory signaling of their WT counterparts.

We engineered Jurkat lines that express similar levels of either WT PD-1 or its mutant in which both intracellular tyrosines (Y223 and Y248) were replaced by phenylalanine (denoted as PD-1[FF]; Fig. 1 A). Both versions of PD-1 were fused with a C-terminal monomeric GFP (mGFP) tag for the IP experiments described below and are referred to as PD-1[WT]–mGFP and PD-1[FF]–mGFP, respectively. As expected, upon incubation with SEE-loaded Raji cells expressing PD-L1 fused with a C-terminal monomeric Cherry (mCherry), Jurkat (PD-1[WT]–mGFP^{+}) cells secreted (56% ± 6%) less IL-2 than Jurkat (PD-1[FF]–mGFP^{+}) cells (Fig. 1 B).

Likewise, to quantify BTLA signaling, we transduced Jurkat cells, which do not express BTLA endogenously (Fig. S1 A), with either BTLA[WT]-mGFP or a signaling-deficient BTLA[FFFF]-mGFP in which all four phosphorylatable tyrosines (Y226, Y243, Y257, and Y282) were mutated to phenylalanine. The two versions of BTLA were expressed at similar levels, and neither affected the expression of CD28 (Fig. 1 C and Fig. S1 B). Upon coculturing with SEE-loaded Raji cells expressing HVEM fused with a C-terminal monomeric Ruby (mRuby), Jurkat (BTLA[WT]-mGFP^{+}) cells produced (77% ± 3%) less IL-2 than Jurkat (BTLA[FFFF]-mGFP^{+}) cells. The latter cells produced indistinguishable levels of IL-2 compared with mock-transduced Jurkat cells that lacked BTLA (Fig. 1 D). This result indicates that BTLA exerts its inhibitory effect largely, if not exclusively, through the four intracellular tyrosines.

CD3ζ phosphorylation is resistant to PD-1– but not BTLA-mediated inhibition

Having established the PD-1 and BTLA effects on IL-2 secretion, we next compared their signaling at the receptor level. We recently reported that PD-1 preferentially inhibits the phosphorylation of CD28 over CD3ζ (Hui et al., 2017). Consistent with this finding, a direct comparison of Jurkat expressing PD-1[WT]–mGFP and Jurkat expressing PD-1[FF]–mGFP showed that PD-1 signaling inhibits CD28 phosphorylation, with little to no effect on CD3ζ phosphorylation (Fig. 1 E).

We next examined if BTLA differs from PD-1 with regard to their effects on CD3ζ and CD28 phosphorylation. We conjugated either BTLA[WT]-mGFP–expressing Jurkat or BTLA[FFFF]-mGFP–expressing Jurkat with SEE-loaded Raji (HVEM-mRuby^{+}) cells
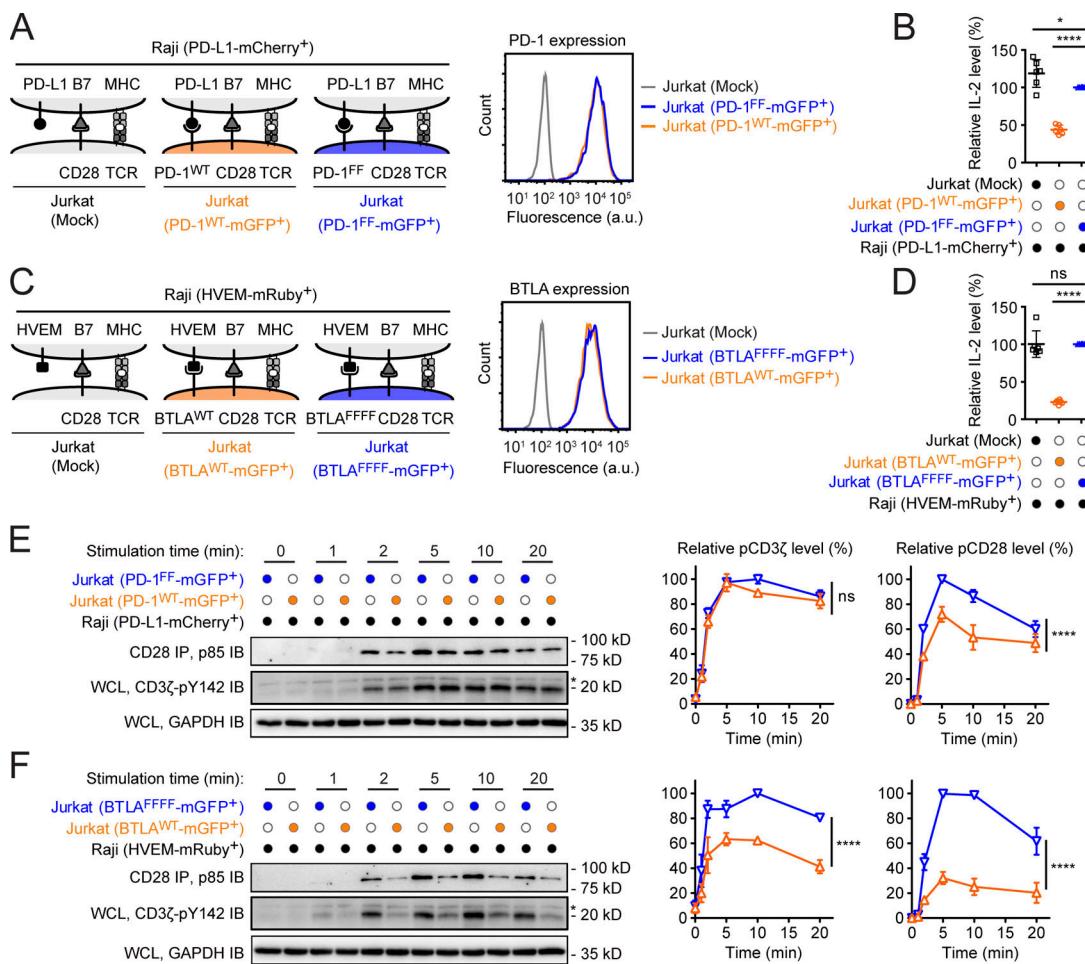
Figure 1. BTLA inhibits Jurkat cells more potently than does PD-1. (A) Left: Cartoons depicting co-culture assays in which indicated types of Jurkat cells were stimulated by SEE-loaded Raji (PD-L1–mCherry⁺) cells. Right: Flow cytometry histograms showing PD-1 surface expressions in the indicated Jurkat T cells. **(B)** Scatter plots showing relative IL-2 levels in the medium of indicated Jurkat-Raji co-cultures. IL-2 levels were normalized to that of Jurkat (PD-1^{FF}–mGFP⁺) cells for each replicate (see Materials and methods). **(C and D)** Same as A and B, except PD-1^{FF}–$mGFP$, PD-1^{WT}–$mGFP$, and PD-$L1$–$mCherry$ were replaced with $BTLA^{FFFF}$-$mGFP$, $BTLA^{WT}$-$mGFP$, and $HVEM$-$mRuby$, respectively. **(E)** Left: Representative IBs showing phospho-CD3ζ (anti-pY142) and phospho-CD28 (coimmunoprecipitated p85) in the lysates of the indicated co-cultures, with the duration of stimulation before lysis indicated (see Materials and methods). The asterisk indicates nonspecific bands. WCL, whole cell lysate. Right: Quantification graphs of phospho-CD3ζ and phospho-CD28, incorporating results from three independent experiments. In each replicate, data were normalized to the highest phosphorylation level under Jurkat (PD-1^{FF}–mGFP⁺) or Jurkat (BTLA^{FFFF}-mGFP⁺) conditions, respectively. **(F)** Same as E, except PD-1^{FF}–$mGFP$, PD-1^{WT}–$mGFP$, and PD-$L1$–$mCherry$ were replaced with $BTLA^{FFFF}$-$mGFP$, $BTLA^{WT}$-$mGFP$, and $HVEM$-$mRuby$, respectively. Data in this figure are presented as means ± SD. *, $P < 0.05$; ****, $P < 0.0001$. Student's t test for B and D ($n = 6$); two-way ANOVA for E and F ($n = 3$). ns, not significant.

and lysed the conjugates at the indicated time points. Subsequent immunoblotting (IB) showed that Raji cells induced a time-dependent phosphorylation of both CD3ζ and CD28. Due to the lack of reliable phospho-CD28 antibodies, we probed CD28 phosphorylation by its associated p85, which binds to a phosphotyrosine (pY) motif within CD28 (Truitt et al., 1994). Notably, phosphorylation of both CD3ζ and CD28 in BTLA^{WT}-mGFP–expressing Jurkat was markedly weaker compared with BTLA^{FFFF}-mGFP (Fig. 1 F). These results demonstrate that unlike PD-1, BTLA potently inhibits the phosphorylation of both TCR and CD28.

BTLA expression in Jurkat cells, compared with PD-1 expression, resulted in a more robust inhibition of IL-2 production and CD28 phosphorylation (Fig. 1 D versus Fig. 1 B, and Fig. 1 F versus Fig. 1 E). This observation could, in principle, be due to a

higher expression level for BTLA than for PD-1. To clarify this issue, we quantified BTLA^{WT}-mGFP and PD-1^{WT}–mGFP expressions using purified mGFP as a standard (Fig. S1 C). This experiment revealed that PD-1 expression was fivefold higher than BTLA expression in the transduced Jurkat cells. Furthermore, in the respective Raji APCs, PD-L1 was more highly expressed than HVEM (Fig. S1 D). The lower expression yet stronger inhibitory effects of BTLA suggests that BTLA is intrinsically more inhibitory than PD-1.

PD-1 recruits SHP2 but not SHP1, whereas BTLA recruits both in T cells

To investigate the mechanism underlying the different potency and specificities of BTLA and PD-1 in T cell suppression, we examined the landscape of intracellular effector proteins recruited

to either BTLA or PD-1. We used the GST-tagged, prephosphory-lated tail of either PD-1 or BTLA to capture proteins from Jurkat lysates and defined their interactomes using mass spectrometry (MS; Meng et al., 2018; Peled et al., 2018). One-sided volcano plots revealed that PD-1 and BTLA both pulled down SHP1 and SHP2. Several other SH2 proteins are also among the top hits. Interest-ingly, ZAP70 coprecipitated with BTLA but not PD-1, whereas signaling lymphocytic activation molecule-associated protein (SAP) and p85 (regulatory subunit of PI3 kinases) coprecipitated with PD-1 (Fig. 2 A).

To validate these interactors in a more physiological setting, we immunoprecipitated either PD-1^{WT}–mGFP or BTLA^{WT}–mGFP from the lysates of Raji-Jurkat co-cultures using an anti-GFP nanobody. Using IB, we detected SHP2 but not SHP1 in the PD-1^{WT}–mGFP precipitate and, in contrast, more SHP1 than SHP2 in the BTLA^{WT}-mGFP precipitate (Fig. 2, B and C). Com-parison of different time points showed that SHP1/2 recruit-ments occurred transiently: peaked at 5 min and decreased to basal levels by 20 min after Raji-Jurkat contact. From 2 to 10 min, BTLA recruited twofold to threefold more SHP1 than SHP2. By contrast, ZAP70, SAP, C-terminal Src kinase (CSK), GRB2, and p85 were undetectable in either PD-1 or BTLA pre-cipitates over the time course examined (Fig. 2 B), indicating that although some of these proteins may interact with PD-1 or BTLA under certain circumstances, the affinities are likely weak.

To examine PD-1/BTLA interactions with SHP1/2 in intact T cells, we used a ligands-reconstituted planar lipid bilayer (PLB) to trigger either PD-1 or BTLA microclusters in OT-1 CD8$^+$ T cells and visualized SHP1 or SHP2 recruitment using total internal reflection fluorescence (TIRF) microscopy. Peptide-bound major histocompatibility complex (pMHC) and PD-L1 functionalized PLB triggered PD-1 microclusters that strongly enriched SHP2 but not SHP1 (Fig. 2 D), consistent with a previous study using CD4$^+$ T cells (Yokosuka et al., 2012). In contrast, pMHC/HVEM–containing PLB triggered BTLA microclusters that enriched SHP1, consistent with a recent study (Mintz et al., 2019), and to a lesser extent SHP2 (Fig. 2 D). Pearson's correlation co-efficients (PCCs) indicate that BTLA:SHP1 colocalization was weaker than PD-1:SHP2 colocalization, consistent with the coIP results (Fig. 2 C).

PD-1 does not recruit SHP1 even in SHP2-deficient T cells
The little to no PD-1:SHP1 association detected could be due to competition from SHP2, as indicated by a recent study (Celis-Gutierrez et al., 2019). To test this idea, we asked whether PD-1 recruits SHP1 in SHP2-deficient T cells. We deleted SHP2 from Jurkat cells via the CRISPR/Cas9 system and transduced the cells with either *PD-1^{WT}–mGFP* or *BTLA^{WT}–mGFP*. Upon stimulation of SHP2 KO Jurkat (PD-1^{WT}–mGFP$^+$) cells with SEE-loaded Raji (PD-L1–mCherry$^+$) cells, we detected minimal SHP1 in GFP IP (Fig. 3 A). By contrast, upon stimulation of SHP2 KO Jurkat (BTLA^{WT}–mGFP$^+$) cells by SEE-loaded Raji (HVEM-mRuby$^+$) cells, we detected a strong SHP1 signal in GFP IP (Fig. 3 A). One caveat of the above experiment is that Raji cells express SHP2, which might have competitively disrupted PD-1:SHP1 associa-tion after cell lysis. Thus, as a further test, we deleted SHP2 from both Raji and Jurkat cells and repeated the foregoing co-culture

assays. Again, SHP1 was detected only in BTLA-mGFP but not PD-1–mGFP precipitates (Fig. 3 B). Consistent with the coIP re-sults, weak to no SHP1 recruitment to PD-1 microclusters was observed in PD-L1 PLB–stimulated SHP2 KO Jurkat cells over the entire time course of acquisition (Fig. 3 C, upper row; and Video 1). By contrast, PD-1 microclusters strongly recruited SHP2 in SHP1 KO Jurkat cells (Fig. 3 C, lower row; and Video 1), as expected. Taken together, these data indicate that the lack of a PD-;1:SHP1 association in T cells (Fig. 2, B and C; and Fig. 3, A–C) was due to intrinsic instability of the interaction rather than competition from SHP2.

We did note that the SHP1 IB signal appeared to precede the pY IB signal in Fig. 3, A and B, suggesting distinct pY spe-cificities of SHP1 and the anti-pY antibody. To test this directly, we constructed and purified a mutant BTLA intracellular tail (BTLA^{INT}) containing each of the four tyrosines (Y226, Y243, Y257, or Y282), each prephosphorylated with purified Lck, and determined the binding preference of anti-pY. IB revealed that anti-pY preferred pY226 and pY243 over pY257 and pY282 (Fig. S2), consistent with peptide microarray profiling (Tinti et al., 2012). Thus, it is likely that in SHP2 KO Jurkat (BTLA^{WT}-mGFP$^+$) cells, phosphorylation of the SHP1 docking sites Y257 and Y282 occurred faster than the anti-pY docking sites pY226 and pY243, leading to the observed earlier onset of SHP1 signal.

The intracellular tails of BTLA and PD-1 dictate their specificities
The above experiments show that PD-1 and BTLA exhibit dis-tinct binding specificities to PTPases. In principle, this distinc-tion could be due to either intracellular tails or ectodomains, which engage different ligands. To dissociate the intra- and extracellular contributions, we created Jurkat cells expressing a PD-1:BTLA chimera comprising PD-1$^{ECTO-TMD}$, BTLA^{INT}, and a C-terminal mGFP tag (PD-1$^{ECTO-TMD}$–BTLA^{INT}–mGFP$^+$; Fig. 4 A), such that BTLA intracellular signaling can be triggered by PD-L1. Moreover, flow cytometry showed that this chimeric receptor was expressed in a similar amount as PD-1^{WT}–mGFP and PD-1^{FF}–mGFP in their respective host Jurkat cells (Fig. 4 B), thus allowing for direct comparison of PD-1^{INT} and BTLA^{INT} in the Raji-Jurkat co-culture assay. Upon conjugation of the respective Jurkat cells with Raji (PD-L1–mCherry$^+$) cells, both PD-1^{WT}–mGFP and PD-1$^{ECTO-TMD}$–BTLA^{INT}–mGFP became tyrosine phosphory-lated (Fig. 4 C; GFP IP, pY IB) and recruited SHP2 (Fig. 4 C; GFP IP, SHP2 IB). By contrast, SHP1 was recruited by PD-1$^{ECTO-TMD}$–BTLA^{INT}–mGFP but not by PD-1^{WT}–mGFP (Fig. 4 C; GFP IP, SHP1 IB). Thus, BTLA^{INT} is sufficient to recruit SHP1, even when fused to the PD-1$^{ECTO-TMD}$.

In the reciprocal experiment, we generated Jurkat cells ex-pressing a BTLA:PD-1 chimera consisting of BTLA$^{ECTO-TMD}$, PD-1^{INT}, and a C-terminal mGFP (BTLA$^{ECTO-TMD}$–PD-1^{INT}–mGFP$^+$; Fig. 4 D). This chimera was expressed at a similar level as BTLA^{WT}–mGFP in their respective host Jurkat cells (Fig. 4 E). Upon incubation with Raji (HVEM-Ruby$^+$) cells, BTLA$^{ECTO-TMD}$–PD-1^{INT}–mGFP became phosphorylated, akin to BTLA^{WT}–mGFP (Fig. 4 F; GFP IP, pY IB). However, while BTLA^{WT}–mGFP recruited both SHP1 and SHP2, BTLA$^{ECTO-TMD}$–PD-1^{INT}–mGFP recruited SHP2 but not SHP1 (Fig. 4 F; GFP IP, SHP2 IB), further supporting
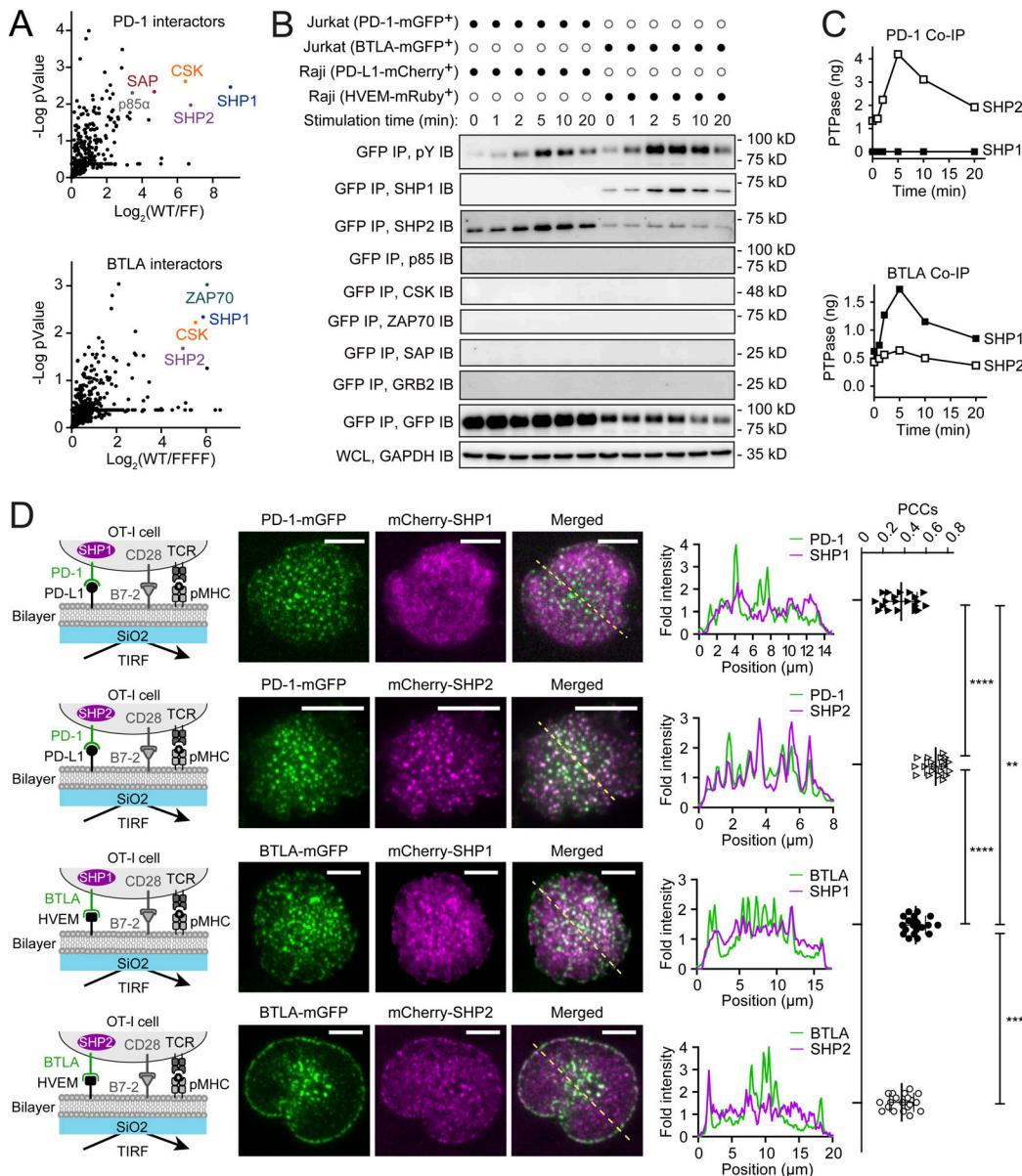
Figure 2. **PD-1 recruits SHP2 but not SHP1, whereas BTLA recruits both in T cells. (A)** One-sided volcano plot showing MS-identified proteins in GST–PD-1[INT] or GST-BTLA[INT] pull-down samples (see Materials and methods). SH2 domain-containing proteins are labeled. **(B)** Representative IBs showing the levels of phosphotyrosine (pY IB) and GFP (GFP IB) in PD-1–mGFP or BTLA-mGFP immunoprecipitate (GFP IP), as well as the coprecipitated SHP1, SHP2, p85, CSK, ZAP70, SAP, and GRB2 from the indicated co-culture lysates, with the duration of stimulation before the lysis indicated (see Materials and methods). GAPDH IB indicates the input of each sample. **(C)** Coprecipitated SHP1 and SHP2 in B were quantified using purified recombinant SHP1 or SHP2 standards and plotted as SHP1 versus SHP2 recruitments against the stimulation time. **(D)** OT-1–PLB assays showing the recruitment of SHP1 or SHP2 by PD-1 or BTLA in OT-1 cells. Leftmost are cartoons depicting indicated types of OT-1 cells interacting with PLB containing pMHC, CD86, and either PD-L1 or HVEM. Middle left are representative TIRF images of the indicated channels. Scale bars, 5 μm. Middle right are plots of fold intensities along the yellow diagonal line in the overlaid images calculated as described (Yokosuka et al., 2012). Rightmost are PCCs showing the colocalization scores of mGFP microclusters versus mCherry microclusters (see Materials and methods). **, $P < 0.01$; ***, $P < 0.001$; ****, $P < 0.0001$. Student's t test ($n = 20$). WCL, whole cell lysate.

the model that PD-1 does not recruit SHP1. Moreover, similar to WT PD-1, this PD-1[INT]–containing chimera recruited more SHP2 than did BTLA[WT]. Of note, in experiments involving either chimera, decrease in CD3ζ phosphorylation only occurred when the receptor contained an intact BTLA[INT] (Fig. 4, C and F; WCL, CD3ζ-pY142 IB). This result further supports the model that BTLA, but not PD-1, potently inhibits TCR phosphorylation via its associated SHP1.

SHP1 possesses higher intrinsic PTPase activity than SHP2

In the chimera experiments, reduction in CD3ζ phosphorylation correlated with recruitment of SHP1, but not of SHP2. This finding indicates that SHP1 is a more potent PTPase than SHP2. To test this notion, we compared the activities of the PTPase domains of SHP1 and SHP2 using a membrane reconstitution assay with a fluorescence resonance energy transfer (FRET) readout. Specifically, decahistidine (His10)-tagged CD3ζ[INT]
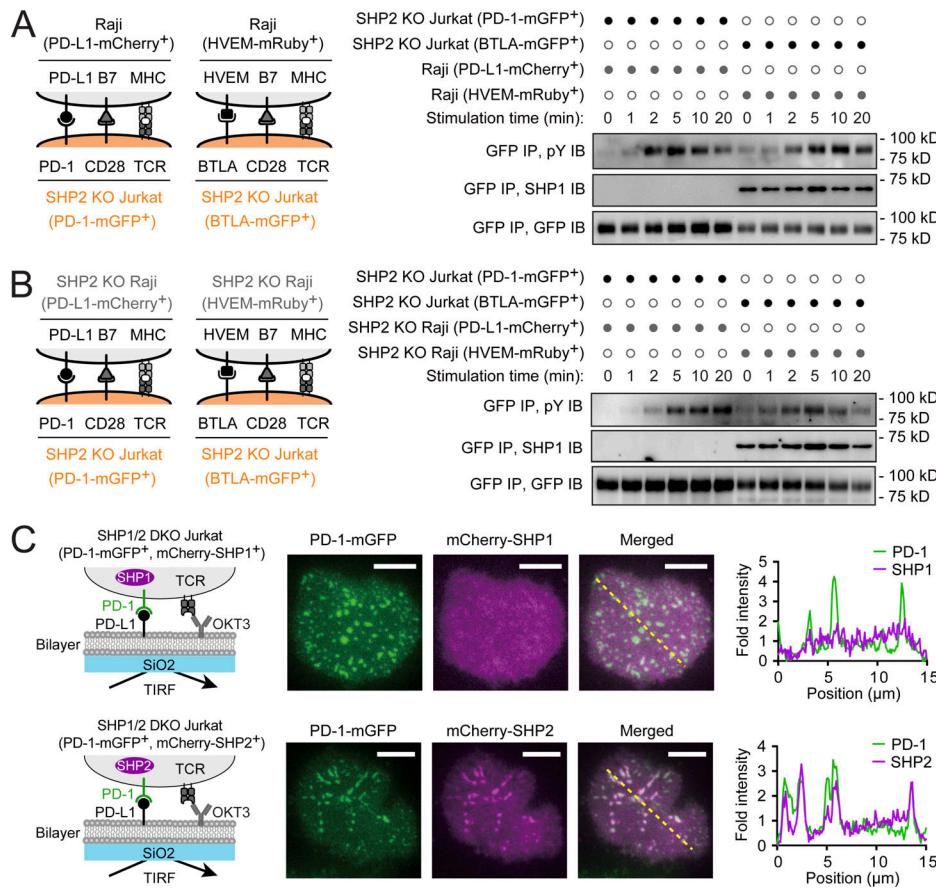
Figure 3. PD-1 does not recruit SHP1 even in SHP2-deficient T cells. (A) Left: Cartoons illustrating Raji-Jurkat co-culture assays in which SHP2 KO Jurkat (PD-1–mGFP[+]) or Jurkat (BTLA-mGFP^{+}) cells were stimulated with SEE-pulsed Raji (PD-L1–mCherry[+]) or Raji (HVEM-mRuby^{+}) cells. Right: Representative IBs of phosphotyrosine (pY IB) and GFP (GFP IB) of PD-1–mGFP or BTLA-mGFP IP (GFP IP) and the coprecipitated SHP1 from the indicated co-culture lysates, with the duration of stimulation before lysis indicated (see Materials and methods). **(B)** Same as A, except SHP2 KO Raji (PD-L1–mCherry^{+}) cells or SHP2 KO Raji (HVEM-mRuby^{+}) cells were used. **(C)** Jurkat-PLB assays showing the degree of recruitment of SHP1 or SHP2 to PD-1 microclusters. Left: Cartoons depicting the indicated type of Jurkat cell interacting with a PLB containing OKT3 and PD-L1. Middle: Representative TIRF images of the indicated channels. Scale bars, 5 μm. Right: Plots showing fold intensities of the indicated channels along the yellow diagonal line in the overlaid images (see Materials and methods).

(substrate), Lck (kinase), and SHP1[PTPase] or SHP2[PTPase] were coattached to large unilamellar vesicles (LUVs) containing His-tag–chelating-lipid DGS-NTA-Ni and Rhodamine (energy acceptor)-labeled phosphorylethanolamine (Rhod-PE). The addition of ATP triggered Lck-mediated phosphorylation of CD3ζ[INT], creating substrates for SHP1[PTPase] or SHP2[PTPase]. The opposing actions of Lck and the PTPase dictated the level of CD3ζ[INT] phosphorylation, which we probed with SNAP-cell-505 (energy donor)–labeled ZAP70 tSH2 domains (SC505*ZAP70[tSH2]). The fluorescence of this reporter would decrease upon its binding to phospho-CD3ζ[INT] due to energy transfer to Rhod-PE (Hui and Vale, 2014). In the absence of SHP1[PTPase] or SHP2[PTPase], ATP led to a maximal CD3ζ[INT] phosphorylation and robust quenching of SC505*ZAP70[tSH2] (Fig. 5 A). SHP1[PTPase] titration decreased the FRET signal with a half-maximal inhibitory concentration (IC$_{50}$) of ~300 nM (Fig. 5 B, blue), whereas SHP2[PTPase] titration revealed an IC$_{50}$ of ~1300 nM (Fig. 5 B, black). In a similar system using CD28[INT] as the substrate, SHP1[PTPase] also exhibited a much lower IC$_{50}$ (~33 nM) than SHP2[PTPase] did (~195 nM; Fig. 5, C and D). The IC$_{50}$ values for both PTPases were much lower in the CD28 system than in the CD3ζ system, likely due to CD28 being a

weaker Lck substrate than CD3ζ (Hui et al., 2017). Furthermore, in both the CD3ζ[INT]/Lck/SHP1[PTPase] system and the CD3ζ[INT]/Lck/SHP2[PTPase] system, disruption of Lck activity by the ATP scavenger apyrase led to dequenching of SC505*ZAP70[tSH2] due to CD3ζ[INT] dephosphorylation by the PTPase (Fig. 5 E). Notably, the dequenching rate was much faster with SHP1[PTPase] than with SHP2[PTPase], further demonstrating that SHP1 possesses a stronger PTPase domain than does SHP2.

BTLA:SHP1, but not BTLA:SHP2 or PD-1:SHP2, inhibits CD3ζ phosphorylation

To further dissect the biochemical specificities of BTLA and PD-1, we next reconstituted a more physiological scenario by (1) using full-length SHP1 or SHP2 to integrate their complex regulatory mechanisms (Lorenz, 2009); (2) using BTLA[INT] or PD-1[INT] to recapitulate the receptor:PTPase interaction; and (3) titrating BTLA[INT] or PD-1[INT] to mimic their various expression levels in vivo. In a reconstitution system in which His$_{10}$-tagged CD3ζ[INT], Lck, and BTLA[INT] were coattached to Rhod-PE LUVs via His:DGS-NTA-Ni interaction and non–His-tagged SHP1 or SHP2 presented in the extravesicular solution, we titrated BTLA[INT]
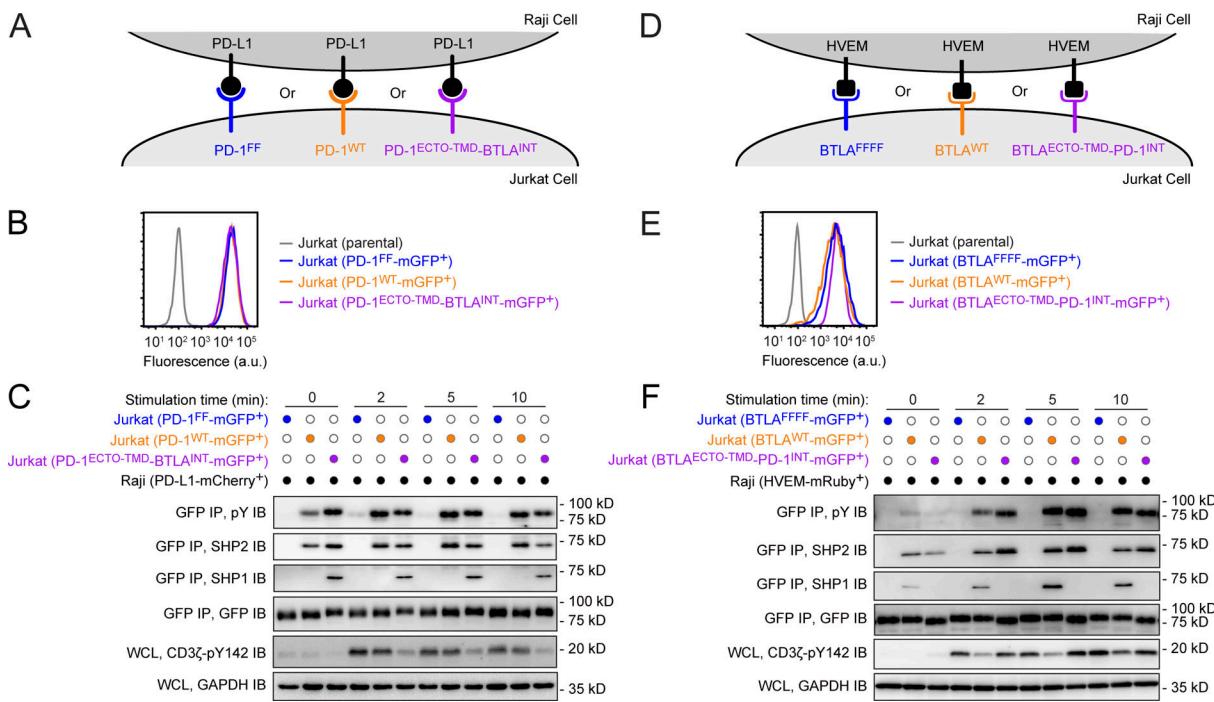
Figure 4. **The intracellular tails of PD-1 and BTLA dictate their specificities. (A)** Cartoon depicting a Raji-Jurkat co-culture assay in which Jurkat (PD-1^{FF}–mGFP$^+$), Jurkat (PD-1^{WT}–mGFP$^+$), or Jurkat (PD-1$^{ECTO-TMD}$–BTLA^{INT}-mGFP$^+$) cells were stimulated with SEE-loaded Raji (PD-L1–mCherry$^+$) cells. **(B)** Flow cytometry histograms showing PD-1 levels on indicated Jurkat T cells. **(C)** Representative IBs of phosphotyrosine (pY IB), GFP (GFP IB), and the coprecipitated SHP1 and SHP2 of immunoprecipitated GFP-tagged receptors. **(D–F)** Same as A–C, except replacing Raji (PD-L1–mCherry$^+$), Jurkat (PD-1^{FF}–mGFP$^+$), Jurkat (PD-1^{WT}–mGFP$^+$), and Jurkat (PD-1$^{ECTO-TMD}$–BTLA^{INT}-mGFP$^+$) cells with Raji (HVEM-mRuby$^+$), Jurkat (BTLA^{FFFF}-mGFP$^+$), Jurkat (BTLA^{WT}-mGFP$^+$), and Jurkat (BTLA$^{ECTO-TMD}$–PD-1^{INT}-mGFP$^+$) cells, respectively. WCL, whole cell lysate.

and probed CD3ζ^{INT} phosphorylation by using SC505*ZAP70^{tSH2}. This experiment showed that BTLA^{INT} titration reduced both the extent and rate of CD3ζ^{INT} phosphorylation when SHP1 was present, whereas the effects were much weaker when an equal concentration of SHP2 was present (Fig. 5 F), in accordance with the weaker PTPase activity of SHP2. Similar to BTLA^{INT} titration, PD-1^{INT} titration had little effect on CD3ζ^{INT} phosphorylation in the presence of SHP2. Distinct from BTLA^{INT} titration, PD-1^{INT} titration failed to impact CD3ζ^{INT} phosphorylation even in the presence of SHP1 (Fig. 5 G). This latter result was likely due to the inability of PD-1 to recruit SHP1, as we observed in cellular assays (Fig. 2, B–D; and Fig. 3, A–C).

SHP1 and/or SHP2 deletions differentially perturb PD-1 and BTLA functions

The above experiments showed that PD-1 and BTLA primarily couple SHP2 (a weaker PTPase) and SHP1 (a stronger PTPase), respectively, to differentially regulate T cell signaling. We then further tested the PTPase requirements in cells by assessing PD-1– or BTLA-mediated inhibition of TCR/CD28 phosphorylation and IL-2 secretion in different PTPase backgrounds. We generated SHP1 KO, SHP2 KO, and SHP1/SHP2 double KO (SHP1/2 DKO) Jurkat cells (Fig. 6 A) and transduced them with *PD-1^{WT}–mGFP*, *PD-1^{FF}–mGFP*, *BTLA^{WT}–mGFP*, or *BTLA^{FFFF}–mGFP* (Fig. 6 B). Upon stimulation with PD-L1– or HVEM-expressing Raji cells, Jurkat cells became phosphorylated at both CD3ζ and CD28, regardless of the PTPase background (Fig. 6, C–E), but

the magnitude of inhibitory effects exerted by PD-1^{WT}–mGFP or BTLA^{WT}-mGFP varied.

In SHP1 KO Jurkat (Fig. 6 C), both BTLA and PD-1 still inhibited CD28 phosphorylation, but the BTLA effect on CD3ζ phosphorylation was largely abolished, even though SHP2 was recruited by BTLA (see Fig. S4 A). Thus, SHP2 can substitute SHP1 to associate with BTLA for CD28 dephosphorylation. However, SHP2, even coupled with BTLA, had limited effect on CD3ζ phosphorylation. Thus, it was the ability of BTLA to recruit SHP1 rather than SHP2 that allowed BTLA to inhibit CD3ζ phosphorylation. In SHP2 KO Jurkat (Fig. 6 D), BTLA still potently inhibited the phosphorylation of both CD3ζ and CD28, suggesting that SHP2 is largely dispensable for BTLA function. In contrast, the PD-1 effect on CD28 phosphorylation was abolished by SHP2 KO. Thus, SHP2 is essential for PD-1 to suppress CD28 phosphorylation, and SHP1 cannot substitute SHP2 to support PD-1 function, perhaps due to its inability to stably associate with PD-1 (Fig. 3). In SHP1/2 DKO Jurkat cells (Fig. 6 E), both BTLA and PD-1 were phosphorylated upon Raji-Jurkat contact (see Fig. S4 B), but their inhibition of CD3ζ/CD28 phosphorylation was largely abolished.

Further, ELISA revealed a positive correlation between the effects on IL-2 and those on receptor phosphorylation. SHP1 KO weakened the BTLA-mediated inhibition of IL-2 (56% ± 5% inhibition for SHP1 KO versus 77% ± 3% inhibition for WT cells), but not PD-1 (53% ± 9% inhibition for SHP1 KO versus 56% ± 6% inhibition for WT cells; Fig. 6 F; Fig. 1, C and F; Fig. S3 A; and
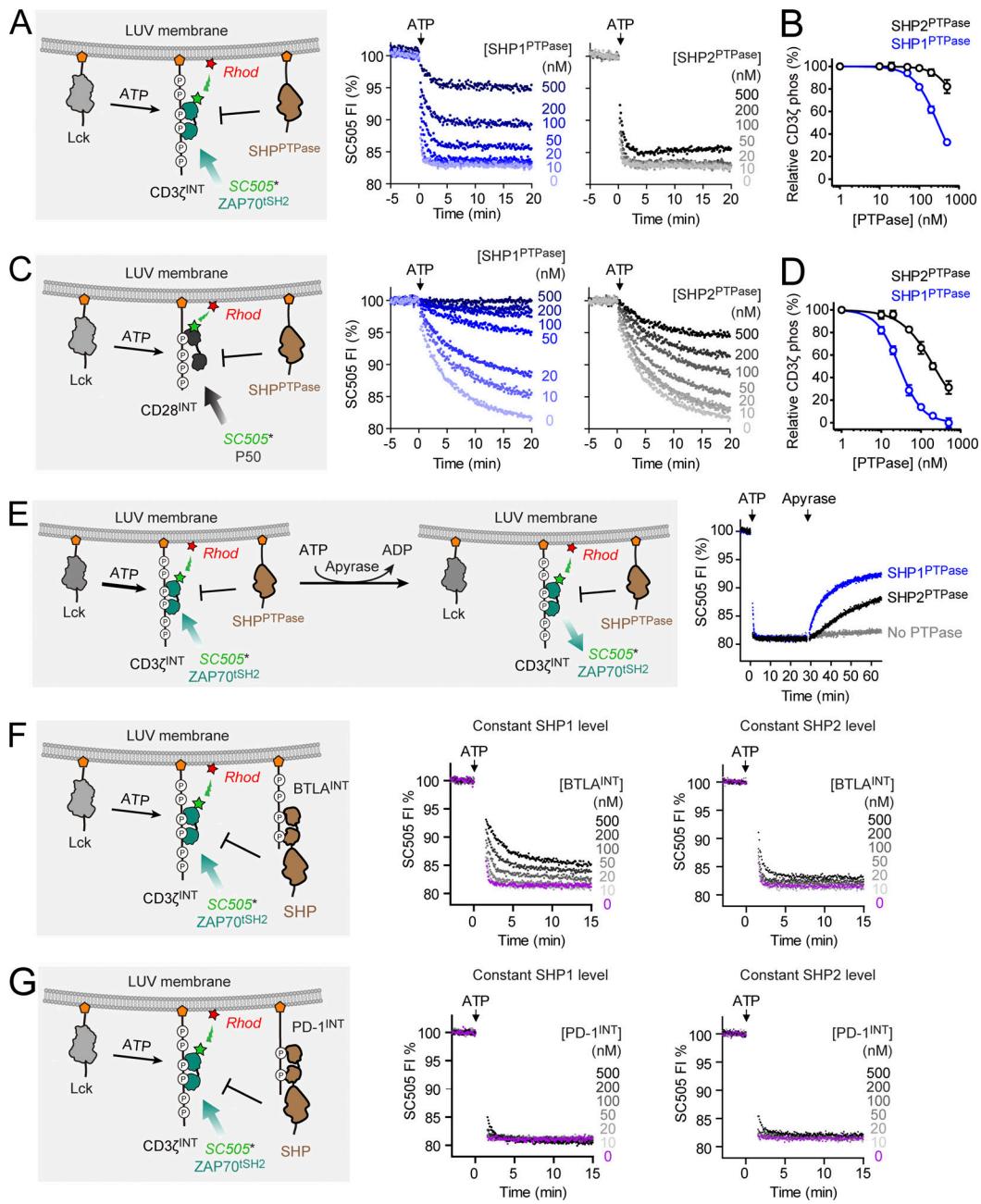
Figure 5.   **SHP1 has a higher phosphatase activity than SHP2. (A)** LUV FRET assays showing PTPase activity of SHP1^{PTPase} or SHP2^{PTPase}. Left: Cartoon depicting a FRET assay for measuring the recruitment of SC505*ZAP70^{tSH2} to LUV-attached Lck-phosphorylated CD3ζ^{INT} in the presence of LUV-attached SHP1^{PTPase} or SHP2^{PTPase} (see Materials and methods). Right: Time courses of ATP-triggered quenching of SC505*ZAP70^{tSH2} at increasing levels of SHP1^{PTPase} or SHP2^{PTPase}. **(B)** Relative CD3ζ phosphorylation, calculated by normalizing the extent of SC505*ZAP70^{tSH2} quenching at 20 min in A to 0 nM SHP1^{PTPase} or SHP2^{PTPase} conditions, were plotted against [SHP1^{PTPase}] or [SHP2^{PTPase}]. Data were fit with "dose response—inhibition" to yield IC$_{50}$ values of SHP1^{PTPase} and SHP2^{PTPase}. **(C and D)** Same as A and B, except replacing CD3ζ^{INT} and SC505*ZAP70^{tSH2} with equal concentrations of CD28^{INT} and SC505*P50. **(E)** Left: Cartoon depicting a FRET assay for probing the activities of SHP1^{PTPase} or SHP2^{PTPase} (50 nM) toward CD3ζ^{INT}. Experiments were set up as in A, except with an apyrase addition step. Right: Representative time courses of SC505 fluorescence intensity (FI) before and after addition of 1 mM ATP and 0.5 U apyrase. **(F)** FRET assays showing how membrane-attached BTLA^{INT} stimulated the ability of SHP1/2 to inhibit CD3ζ^{INT} phosphorylation. Cartoon on the left depicts the assay setup: Lck, CD3ζ^{INT}, and increasing BTLA^{INT} were attached to LUV while SC505*ZAP70^{tSH2} and SHP1 or SHP2 were presented in the extravesicular solution. ATP-triggered phosphorylation of CD3ζ^{INT} and BTLA^{INT}. The prior phosphorylation caused recruitment of SC505*ZAP70^{tSH2} and its quenching due to FRET; the latter phosphorylation led to recruitment of SHP1 or SHP2 that would potentially dephosphorylate CD3ζ^{INT}, measured by SC505*ZAP70^{tSH2} de-quenching. **(G)** Same as E, except replacing BTLA^{INT} with equal concentrations of PD-1^{INT}. Orange pentagons denote His$_{10}$ tags; green stars denote SC505; red stars indicate Rhod-PE; P in white circles indicate phosphotyrosine.
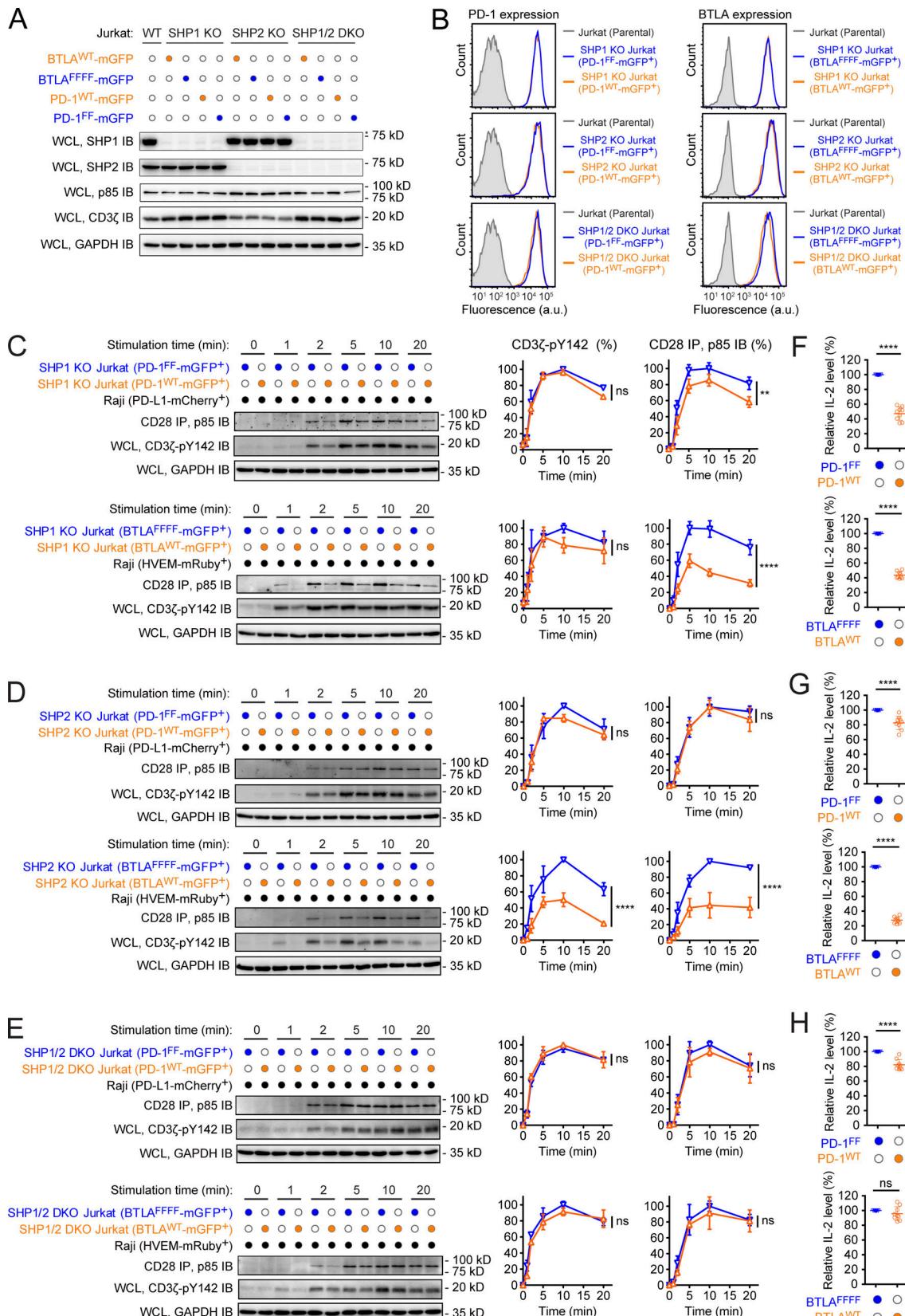
Figure 6. Effects of SHP1 and/or SHP2 deletions on PD-1 and BTLA signaling in Jurkat cells. (A) Representative IBs showing the levels of SHP1, SHP2, p85, and CD3ζ in WT Jurkat cells and *BTLA*WT*-mGFP–*, *BTLA*FFFF*-mGFP–*, *PD-1*WT*–mGFP–*, or *PD-1*FF*–mGFP–*transduced SHP1 KO, SHP2 KO, or SHP1/2 DKO Jurkat cells. GAPDH IB indicates the input of each sample. Asterisk labels nonspecific bands. **(B)** Flow cytometry histograms showing PD-1 (left) or BTLA (right) surface expression in parental Jurkat cells and *PD-1*FF*–mGFP–*, *PD-1*WT*–mGFP–*, *BTLA*FFFF*-mGFP–*, or *BTLA*WT*-mGFP–*transduced SHP1 KO, SHP2 KO, or SHP1/2

DKO Jurkat cells. **(C)** SHP1 KO Jurkat T cells transduced with *PD-1*[FF]*–mGFP, PD-1*[WT]*–mGFP, BTLA*[FFFF]*-mGFP,* or *BTLA*[WT]*-mGFP* were stimulated with SEE-loaded Raji (PD-L1–mCherry[+]) or Raji (HVEM-mRuby^{+}) cells. Left: Representative IBs showing phospho-CD3ζ (anti-pY142) and phospho-CD28 (coimmunoprecipitated p85) in the lysates of the indicated Raji-Jurkat co-cultures, with the duration of the stimulation before lysis indicated (see Materials and methods). Right: Quantification plots of phospho-CD3ζ and phospho-CD28, incorporating results from three independent experiments. In each replicate, data were normalized to the highest phosphorylation level under SHP1 KO Jurkat (PD-1[FF]–mGFP[+]) or SHP1 KO Jurkat (BTLA[FFFF]–mGFP[+]) conditions, respectively. **(D)** Same as C, except using SHP2 KO Jurkat cells. **(E)** Same as C, except using SHP1/2 DKO Jurkat cells. **(F–H)** Scatter plots summarizing relative IL-2 levels in the medium of 6-h Jurkat-Raji co-cultures shown in C–E, respectively. For C–H, data are means ± SD from nine independent experiments. In each replicate, IL-2 levels of Jurkat (PD-1[WT]–mGFP[+]) or Jurkat (BTLA[WT]–mGFP[+]) were normalized to that of Jurkat (PD-1[FF]–mGFP[+]) or to that of Jurkat (BTLA[FFFF]-mGFP[+]) under the same SHP background, respectively (see Materials and methods). **P < 0.01, ****P < 0.0001. Two-way ANOVA for C–E (*n* = 3); Student's *t* test for F–H (*n* = 9). ns, not significant; WCL, whole cell lysate.

Table S1). Conversely, SHP2 KO compromised the IL-2 inhibition effect of PD-1 (17% ± 9% inhibition for SHP2 KO versus 56% ± 6% inhibition for WT cells) but not that of BTLA (72% ± 4% inhibition for SHP2 KO versus 77% ± 3% inhibition for WT cells; Fig. 6 G; Fig. 1, C and F; and Table S1). While this latter result validated SHP2 as a key effector of PD-1, the observed ~17% IL-2 inhibition mediated by PD-1 in SHP2 KO cells indicates the existence of other PD-1 effectors (Fig. 6 G). Notably, we also observed a similar degree of PD-1–mediated inhibition of IL-2 in the SHP1/2 DKO cells (Fig. 6 H and Table S1), suggesting that effectors other than SHP1 mediated this residual inhibitory effect. Notably, we verified these effects of PTPase deletions using Jurkat E6.1 cells purchased directly from ATCC (Fig. S3, B and C).

PD-1 inhibits T cell function in primary T cells lacking both SHP1 and SHP2

We next asked whether the PD-L1:PD-1 axis inhibits the function of SHP1/2 double-deficient primary T cells. We purified SHP1/2 DKO CD8^{+} T cells from *dLck-Cre;Ptpn6*^{fl/fl}*;Ptpn11*^{fl/fl} mice. After validating the lack of both SHP1 and SHP2 in the cells using Western blot (Fig. 7 A), we incubated the cells with beads coated with anti-CD3/anti-CD28 (for TCR/CD28 stimulation) and increasing levels of mouse PD-L1–Fc fusion protein (for PD-1 stimulation), using IgG as a filler protein. IL-2 was included in the medium to improve cell viability. SHP1/2 DKO CD8^{+} T cells expressed PD-1 throughout the time course of bead stimulation with a peak expression at 48 h (Fig. 7 B). Using CellTrace Violet (CTV) assay, we found that anti-CD3/anti-CD28/IgG beads stimulated the proliferation of SHP1/2 DKO CD8^{+} T cells at 48 and 72 h, and this effect was inhibited by PD-L1 in a dose-sensitive manner at both time points (Fig. 7 C). Anti-CD3/anti-CD28/IgG beads also increased the abundance of IL-2^{+} T cells, and IFN-γ^{+} T cells at 24 and 48 h, as revealed by flow cytometry (Fig. 7, D and E). Inclusion of PD-L1 dose-dependently decreased these effects at both time points (Fig. 7, D and E). In both proliferation and cytokine assays, the PD-L1 inhibitory effect appeared to be more pronounced at earlier time points (Fig. 7, C–E).

In parallel, we investigated the PD-L1 effect using WT CD8^{+} T cells derived from the *Ptpn6*^{fl/fl}*;Ptpn11*^{fl/fl} littermates. As expected, anti-CD3/anti-CD28/IgG beads stimulated cell proliferation at both 48 h and 72 h, and PD-L1 inhibited proliferation at both time points (Fig. 7 F). Likewise, anti-CD3/anti-CD28/IgG beads enriched IL-2^{+} and IFN-γ^{+} cells at 24 and 48 h (Fig. 7, G and H), and PD-L1 inhibited these effects. Even in the absence of PD-L1, proliferation and cytokine production of WT CD8^{+} cells

occurred in a much slower and modest fashion compared with the SHP1/2 DKO cells, presumably due to inhibitory effects exerted by SHP1 and/or SHP2 via mechanisms independent of PD-L1:PD-1 ligation. PD-L1–mediated inhibitory effects appeared to be less dose sensitive and more persistent in WT cells compared with those in SHP1/2 DKO cells, despite lower PD-1 expression on WT cells than on SHP1/2 DKO cells (Fig. 7 B).

Finally, inclusion of HVEM-Fc on anti-CD3/anti-CD28 beads also inhibited the proliferation and cytokine production of both SHP1/2 DKO and WT CD8^{+} T cells, with a more persistent effect on the latter (Fig. S5). In the SHP1/2 DKO background, PD-L1– and HVEM-mediated inhibitory effects appeared to be more evident in primary CD8^{+} T cells than in Jurkat cells. The exact reason is unclear but might be due to the lack of SH2 domain-containing inositol phosphatase 1 (SHIP1) or other inhibitory molecules in Jurkat cells (Lo et al., 2009).

Collectively, data presented in this section validated that both PD-L1:PD-1 and HVEM:BTLA can inhibit T cell functions in a SHP1/2–independent fashion, but SHP1/2 promote optimal functions of PD-L1:PD-1 and HVEM:BTLA, allowing them to more potently and persistently inhibit T cell activity.

Discussion

In this work, we systematically compared PD-1 and BTLA signaling using quantitative biochemistry and cell biology approaches. Our results uncovered multiple layers of distinctions between these two coinhibitory receptors. First, despite the similarities in their inhibitory motifs, PD-1 and BTLA exhibit distinct binding specificities to PTPases: while PD-1 selectively recruits SHP2 over SHP1, BTLA preferentially recruits SHP1 over SHP2. Second, the HVEM:BTLA axis more potently inhibits IL-2 production than does the PD-L1:PD-1 axis at a per-receptor level. Third, the BTLA:SHP1 complex is more inhibitory than the BTLA:SHP2 or PD-1:SHP2 complex due to the stronger PTPase activity of SHP1. Additionally, we showed that PD-1 can function partially through a mechanism independent of both SHP1 and SHP2.

Our finding of PTPase preferences of PD-1 and BTLA is in general agreement with two recent studies (Celis-Gutierrez et al., 2019; Mintz et al., 2019). The distinct PTPase preferences might avoid the competition of PD-1 and BTLA, thus forming the basis for their functional synergy (Fourcade et al., 2012; Grabmeier-Pfistershammer et al., 2017; Zhao et al., 2016). The PD-1:SHP2 complex and BTLA:SHP1 complex can thus form independently and work in concert to suppress T cell activity.

Xu et al.
Comparative analysis of PD-1 and BTLA signaling

Journal of Cell Biology 10 of 20
https://doi.org/10.1083/jcb.201905085
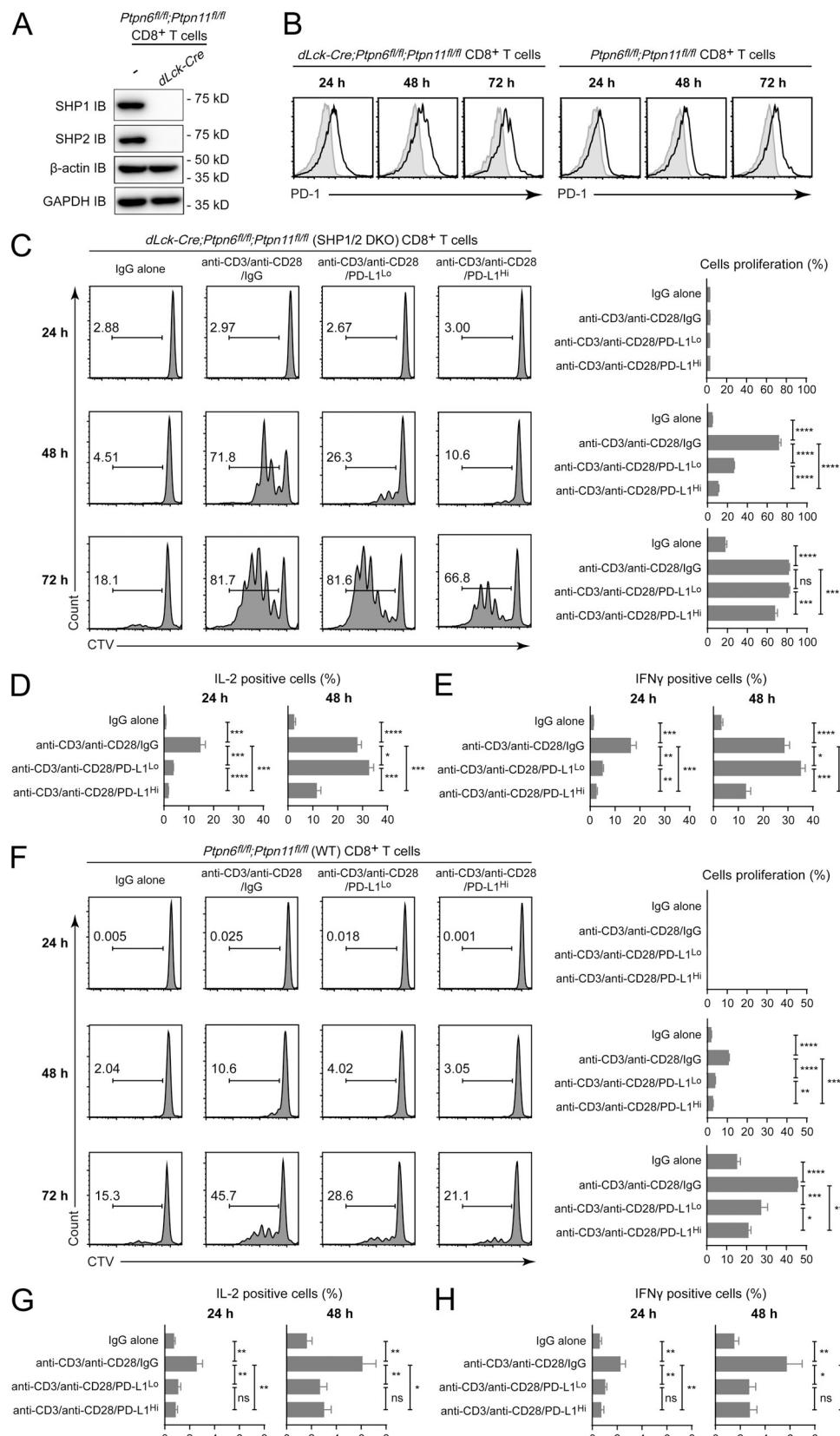
Figure 7. PD-L1 inhibits the functions of mouse primary T cells deficient in both SHP1 and SHP2. (A) IBs validating the lack of SHP1 and SHP2 expression in *dLck-Cre; Ptpn6*^fl/fl^; *Ptpn11*^fl/fl^ (SHP1/2 DKO) CD8^+^ T cells freshly isolated from *dLck-Cre;Ptpn6*^fl/fl^;*Ptpn11*^fl/fl^ mice. β-actin and GAPDH IBs indicate the input of each sample. **(B)** Flow cytometry histograms showing PD-1 surface expression (black traces) in SHP1/2 DKO CD8^+^ T cells at 24, 48, and 72 h after stimulation. Gray traces correspond to isotype antibody–stained cells. **(C)** SHP1/2 DKO CD8^+^ T cells were stained with CTV dye and stimulated with protein G Dynabeads

precoated with IgG alone, anti-CD3/anti-CD28/IgG, anti-CD3/anti-CD28/PD-L1–Fc^{low}, or anti-CD3/anti-CD28/PD-L1–Fc^{high}, respectively (see Materials and methods). Flow cytometry diagrams on the left show the degrees of CTV dilution as a consequence of cell proliferation at 24, 48, and 72 h under the indicated stimulation condition. The number denotes percentage of proliferating cells. Bar graphs on the right summarize the percentage of proliferating cells in three technical replicates. **(D)** Percentage of IL-2–positive cells 24 and 48 h after the indicated stimulation, measured by flow cytometry. **(E)** Percentage of IFN-γ$^+$ cells 24 and 48 h after the indicated stimulation, measured by flow cytometry. **(F–H)** Same as C–E, except using WT CD8$^+$ T cells freshly isolated from $Ptpn6^{fl/fl};Ptpn11^{fl/fl}$ mice. Data in this figure are presented as means ± SD. *, P < 0.05; **, P < 0.01; ***, P < 0.001; ****, P < 0.0001. ns, not significant; Student's t test ($n = 3$).

PTPase specificities of other ITIM/ITSM–containing receptors should be worthwhile to study in the future.

Despite the general consensus that PD-1 signals primarily through SHP2 (Hui et al., 2017; Okazaki et al., 2001; Yokosuka et al., 2012), Guarda and colleagues recently reported that PD-1 blockade enhances tumor control in T cell–specific SHP2 KO mice (Rota et al., 2018), indicating that PD-1 can exert its inhibitory effects in the absence of SHP2 in vivo. The more recent model that SHP1 supports PD-1 function in the absence of SHP2 is straightforward (Celis-Gutierrez et al., 2019); however, multiple assays reported here found no evidence that SHP1 is biochemically involved in PD-1 signaling, even in SHP2 KO cells. Consistent with these results, PD-1 retained its full capacity to inhibit IL-2 production in SHP1 KO cells, and PD-1 activity was similar in SHP2 KO and SHP1/2 DKO Jurkat cells (Fig. 6, F–H; and Table S1). Thus, our data collectively suggest that SHP1 does not display a significant role in supporting PD-1 function. The inability for SHP1 to stably associate with PD-1 in T cells might be attributed to its 97% lower PD-1 affinity than that of SHP2 (Hui et al., 2017), in conjunction with SHP1-mediated PD-1 dephosphorylation (Goyette et al., 2017). Related to the latter notion, we recently showed that SHP2 dephosphorylates PD-1 to disassemble the PD-1:SHP2 complex (Hui et al., 2017). Conceivably, the higher PTPase activity of SHP1 would render the PD-1:SHP1 complex highly labile, except in the presence of phosphatase inhibitors as in a typical coIP assay.

Importantly, our experiments with both engineered Jurkat cell lines and mouse primary T cells suggest the existence of SHP1/2–independent mechanism(s) of PD-1 and BTLA signaling. While SHP2 clearly contributes to optimal PD-1 functions, in agreement with previous studies (Hui et al., 2017; Okazaki et al., 2001; Yokosuka et al., 2012), we found that PD-1 still inhibited the proliferation and IL-2 production of SHP1/2 DKO CD8$^+$ T cells, despite a more transient fashion than in WT CD8$^+$ T cells. One limitation of our primary T cell experiments is that PD-1 expression was higher in the SHP1/2 DKO cells than in the WT cells, making it difficult to draw a quantitative conclusion; nevertheless, the key finding is that PD-1 remained inhibitory in the SHP1/2 DKO background. The exact mechanism by which PD-1 inhibits T cell functions in the absence of SHP1 and SHP2 is unknown. Presumably, other inhibitory molecules, especially those containing SH2 domains, might contribute to PD-1 functions. Mechanisms independent of pY:SH2 interactions are also possible. Along this line, PD-1 reportedly increases phosphatase and tensin homolog activity (Patsoukis et al., 2013), although it is unclear whether SHP2 is required for this effect. The PD-1 and BTLA interactomes reported here and elsewhere (Celis-Gutierrez et al., 2019; Meng et al., 2018; Peled et al., 2018) might help define the elusive SHP1/2–independent mechanism(s).

Compared with the strict commitment to SHP2 by PD-1, BTLA is more promiscuous in that it stably recruits both SHP1 and SHP2, though both interactions appear to be weaker than the PD-1:SHP2 interaction. How SHP1 docking sites within BTLA survive SHP1-mediated dephosphorylation warrants further investigation. The indistinguishable IL-2 secretion from WT and SHP2 KO Jurkat cells suggests that BTLA primarily functions through SHP1, consistent with a recent in vivo study (Mintz et al., 2019). However, BTLA only displayed a modest defect in IL-2 inhibition in SHP1 KO cells, suggesting that SHP2 can partially support BTLA function. Previous work indicates that BTLA:SHP1 and BTLA:SHP2 interactions both require dual phosphorylation of Y257 and Y282 (Gavrieli et al., 2003). It is likely that SHP1 and SHP2 compete for BTLA in WT T cells, and the prior dominates perhaps due to its higher expression in T cells (Hukelmann et al., 2016; Rieckmann et al., 2017).

Using reconstitution assays, we deconstructed BTLA signalosomes into BTLA:SHP1 and BTLA:SHP2 axes. Quantitative activity assays revealed that the BTLA:SHP1 complex is much more inhibitory than the BTLA:SHP2 complex and also the PD-1:SHP2 complex due to the superior PTPase activity of SHP1. Thus, the ability of BTLA to recruit SHP1 is in line with its more potent inhibition of IL-2 production versus PD-1 in our cell culture assays. The superior inhibitory activity of BTLA over PD-1 might be surprising in the context of more severe autoimmunity associated with PD-1 KO (Iwai et al., 2017; Nishimura et al., 1999; Nishimura et al., 2001) and the more impressive clinical activities of PD-1 inhibitors (Herbst et al., 2014; Topalian et al., 2012). However, spatiotemporal expressions of PD-1, BTLA, their ligands, and counter-receptors might influence their in vivo functions. In particular, while PD-1 is best known for inhibiting the effector phase of the T cell response, BTLA might largely inhibit T cell priming with decreased function at the effector stage due to down-regulation (Baitsch et al., 2012; Hurchla et al., 2005), unless under pathological conditions in which BTLA is constitutively elevated (Derré et al., 2010; Pasero and Olive, 2013; Zhao et al., 2016). Additionally, the HVEM:BTLA axis might be more effectively restricted by cis-interactions (Cheung et al., 2009) or compensated by the inhibitory HVEM:CD160 axis (Cai et al., 2008).

For both PD-1 and BTLA, CD28 phosphorylation was more markedly inhibited than for CD3ζ. Given that phosphorylation is reciprocally controlled by kinases and phosphatases, stronger kinase substrates would be more resistant to phosphatase activities. We recently showed that even though SHP2 has similar PTPase activities toward CD28 and CD3ζ, the latter is a better substrate for Lck, rendering it more resistant to SHP2 activity (Hui et al., 2017). We have now shown that this is true regardless of whether SHP2 is coupled to PD-1 or BTLA. By contrast, the

BTLA:SHP1 complex inhibited CD3ζ phosphorylation, presumably due to the ability of SHP1 to dominate Lck. A general implication of our study is that SHP2-recruiting receptors might be mild checkpoints that target weak kinase substrates, such as CD28 and CD226 (Wang et al., 2018), whereas SHP1-recruiting receptors are potent checkpoints that are able to regulate a wider spectrum of signaling molecules.

Materials and methods

List of oligos
A list of oligos is presented in Table 1.

Reagents
For cell culture and transfection, RPMI 1640 (#10-041-CM) was purchased from Corning. DMEM (#25-501) was from Genesee Scientific. 100× penicillin-streptomycin solution (#SV30010) was from GE Healthcare. FBS (#FB-02) was from Omega Scientific. Lipofectamine Transfection Reagent (#18324010) was from Thermo Fisher Scientific.

For preparation of LUVs or small unilamellar vesicles (SUVs), synthetic 1,2-dioleoyl-sn-glycero-3-phosphocholine (POPC; #850457C); 1,2-dioleoyl-sn-glycero-3-[(N-(5-amino-1-carboxypentyl) iminodiacetic acid) succinyl] (nickel salt, DGS-NTA-Ni; #790404C); 1,2-dioleoyl-sn-glycero-3-phosphoethanolamine-N-[methoxy(polyethylene-glycol)-5000] (ammonium salt, PEG5000-PE; #880230C); and N-(lissamine Rhodamine B sulfonyl)-1,2-dipalmitoyl-sn-glycero-3 phosphoethanolamine (Rhod-PE; #810158C) were purchased from Avanti Polar Lipids.

For Jurkat-Raji co-culture assays, PY20 mouse anti-pY antibody (#P4110) was purchased from Sigma-Aldrich. SEE (#ET404) super antigen was from Toxin Technology. Mouse anti-human CD28 antibody (#16-0289-85), rabbit anti-GFP antibody (#A6455), mouse anti-human PD-1 phycoerythrin (PE; #12-9969-42), and Protein G Dynabeads (#10004D) were from Thermo Fisher Scientific. Rabbit anti-human p85 antibody (#4292S) was from Cell Signaling Technology. Mouse anti-human CD3ζ-pY142 antibody (#558489) was obtained from BD Biosciences. GFP-Trap (#gta-20) was obtained from Chromotek. Mouse anti-human SHP1 antibody (#sc-7289), mouse anti-human SHP2 antibody (#sc-7384), mouse anti-human CSK antibody (#sc-166560), mouse anti-human SAP antibody (#sc-393948), and mouse anti-human GRB2 antibody (#sc-8034) were from Santa Cruz Biotechnology. Rabbit anti-GAPDH polyclonal antibody (#10494-1-AP) was from Proteintech Group. Mouse anti-human BTLA PE (#344505), mouse anti-human CD28 Allophycocyanin (#302911), mouse anti-human HVEM Allophycocyanin (#318807), mouse anti-human PD-L1 Allophycocyanin (#393609), and mouse anti-human ZAP-70 antibody (#313402) were purchased from BioLegend.

For mouse CD8+ primary T cell experiments, rat anti-mouse CD4 biotin (#100508), rat anti-mouse CD8 biotin (#100704), rat anti-mouse CD44 biotin (#103004), rat anti-mouse CD45RA/B220 biotin (#103204), rat anti-mouse CD25 biotin (#102004), mouse anti-mouse NK1.1 biotin (#108703), rat anti-mouse CD11b biotin (#101204), Armenian hamster anti-mouse CD11c biotin (#117304) antibody, rat anti-mouse IL-2 FITC (#503806), rat

anti-mouse PD-1 FITC (#135214), rat anti-mouse CD3 (#100331), Syrian hamster anti-mouse CD28 (#102112), and recombinant mouse HVEM-Fc fusion protein (#771306) were purchased from BioLegend. BeaverBeads Streptavidin (#22307-10) was purchased from Beaver Beads. Rat anti-mouse CD8 Allophycocyanin-eFluor 780 (#47-0081-82), rat anti-mouse CD44 eFluor 450 (#48-0441-82), anti-mouse CD44 Allophycocyanin (#17-0441-82), and rat anti-mouse IFN-γ PE (#12-7311-82) were obtained from eBioscience. The CTV Cell Proliferation Kit (#C34557), recombinant mouse IL-2 (#14802164), and Protein G Dynabeads were obtained from Thermo Fisher Scientific. Mouse IgG (#10690-MNAH) and recombinant mouse PD-L1–Fc fusion protein (#50010-M02H) were purchased from Sino Biological. PMA (#P1585-1MG) was from Sigma-Aldrich. Ionomycin (#407950-5MGCN) was from Merck. GolgiStop Protein Transport Inhibitor (#554724) and Fixation/Permeabilization Solution Kit (#554714) were from BD Biosciences.

Cell cultures
Two independent clones of Jurkat E6.1 cells were obtained, from Dr. Arthur Weiss (University of California San Francisco, San Francisco, CA) and from ATCC, respectively. HEK293T cells and Raji B cells were obtained from Dr. Ronald Vale (University of California San Francisco). HEK293T cells were maintained in DMEM (Genesee Scientific; #25-501) supplemented with 10% FBS, 100 U/ml of penicillin, and 100 µg/ml of streptomycin at 37°C/5% CO_2. Jurkat and Raji cells were maintained in RPMI-1640 medium (Corning; #10-041-CM) supplemented with 10% FBS, 100 U/ml of penicillin, and 100 µg/ml of streptomycin at 37°C/5% CO_2. OT-1 splenocytes isolated from C57BL/6-Tg (TcraTcrb) 1100Mjb/J (OT-1) mice (Jackson Laboratory) and mouse primary CD8+ T cells were maintained in RPMI-1640 medium supplemented with 10% FBS, 100 U/ml of recombinant mouse IL-2, 100 U/ml of penicillin, 100 µg/ml of streptomycin, and 50 µM β-mercaptoethanol (β-ME; Thermo Fisher Scientific; #ICN19024283) at 37°C/5% CO_2.

Mice
$Ptpn6^{fl/fl}$ mice were kindly provided by Nicholas R.J. Gascoigne at the National University of Singapore (Singapore). $Ptpn11^{fl/fl}$ mice were a generous gift from Zhongxian Lu at Xiamen University (Fujian, China). $dLck-Cre;Ptpn6^{fl/fl};Ptpn11^{fl/fl}$ mice were bred by Guo Fu's laboratory at Xiamen University. C57BL/6-Tg (TcraTcrb) 1100Mjb/J (OT-1) mice were purchased from Jackson Laboratory. All mouse experiments were approved by the Xiamen University Institutional Animal Care and Use Committee. For all experiments, 8–10-wk-old mice were used.

Recombinant proteins
N-terminal His_{10}-tagged human protein tyrosine kinase Lck (with a G2A mutation to abolish myristoylation) was expressed in the Bac-to-Bac baculovirus system (Hui and Vale, 2014). Human CD28^INT (aa 180–220), CD3ζ^INT (aa 52–164), PD-1^INT (aa 194–288), SHP1^PTPase (aa 243–541), and SHP2^PTPase (aa 246–551) were all expressed with an N-terminal His_{10} tag in Escherichia coli using the pET28A vector. The foregoing His-tagged proteins were purified using the Ni-NTA agarose (Thermo Fisher

Table 1. **List of oligos**

Name	Sequence (5'- to -3')	Purpose	Construct
EH-524	gagctctcgagaattctcacgcgtatgcagatcccacaggcg	Clone human PD-1$^{WT\ or\ FF}$ into pHR-mGFP vector	pHR-PD-1$^{WT\ or\ FF}$-mGFP
EH-863	gcaagcttgatatcctgcagacgcgtcaggggccaagagcagt		
EH-741	gagctctcgagaattctcatgaagacattgcctgccat	Clone human BTLA$^{WT\ or\ FF}$ into pHR-mGFP vector	pHR-BTLA$^{WT\ or\ FF}$-mGFP
EH-742	caagcttgatatcctgcagacgcgtactcctcacacatatggatg		
EH-1004	ctggccgtcatctgctccagaaggcaccaaggaaagc	Pair with EH-742, clone human BTLA^{INT} into pHR-mGFP vector	pHR–PD-1$^{ECTO-TMD}$–BTLA^{INT}-mGFP
EH-1005	ggagcagatgacggccag	Pair with EH-524, clone human PD-1$^{ECTO-TMD}$ into pHR-mGFP vector	
EH-1006	ctgcctgttctgctgcctgcgggccgcacgagggaca	Pair with EH-863, clone human PD-1^{INT} into pHR-mGFP vector	pHR–BTLA$^{ECTO-TMD}$–PD-1^{INT}–mGFP
EH-1007	caggcagcagaacaggcag	Pair with EH-741, clone human BTLA$^{ECTO-TMD}$ into pHR-mGFP vector	
EH-1829	gagctctcgagaattctcacgcgtatgaggatatttgctgtctttatattcatg	Clone human PD-L1 into pHR-mCherry vector	pHR–PD-L1–mCherry
EH-959	caccatggtggcgaccggtggatccgtctcctccaaatgtgtatc		
EH-70	agctctcgagaattctcatggagcctcctggag	Clone human PD-L1 into pHR-mRuby vector	pHR-HVEM-mRuby
EH-71	caagcttgatatcctgcagacggtggtttgggctcctccc		
EH-1391	tggaggctcgagcggtggcggccgcatggtgaggtggtttcaccg	Clone human SHP1 into pHR-mCherry vector	pHR-mCherry-SHP1
EH-1392	cgactctagagtcgcggccgctcacttcctcttgagggaacc		
EH-1078	tggaggctcgagcggtggcggccgcatgacatcgcggagatgg	Clone human SHP2 into pHR-mCherry vector	pHR-mCherry-SHP2
EH-1079	tctagagtcgcggccgcttcatctgaaactttctgctgttg		
EH-396	tctgttccaggggcccctgggatcccgggccgcacgagg	Clone human PD-1$^{INT\ (WT\ or\ FF)}$ into pGEX6p2-GST vector	pGEX6p2-GST–PD-1$^{INT\ (WT\ or\ FF)}$
EH-397	ggccgctcgagtcgacccgggttacaggggccaagagc		
EH-637	ttaactttaagaaggagatataccatgtccccctatactaggt	Clone GST-human BTLA$^{INT\ (WT\ or\ FFFF)}$ into pET28A-TwinStrep vector	pET28A-GST-BTLA$^{INT\ (WT\ or\ FFFF)}$-TwinStrep
EH-607	tccacctttctcgaactgcgggtggctccaggatccactcctcacacatatgg		
EH-1070	gagctctcgagaattctcacgcgtatgtgggtccggcag	Clone mouse PD-1 into pMIG II-mGFP vector	pMIG II-mouse PD-1–mGFP
EH-1071	agcttgatatcctgcagacgcgtaagaggccaagaacaatgtc		
EH-1376	gagctctcgagaattctcacgcgtatgaagacagtgcctgccatg	Clone mouse BTLA into pMIG II-mGFP vector	pMIG II-mouse BTLA-mGFP
EH-1377	caagcttgatatcctgcagacgcgtacttctcacacaaatggatgc		
EH-1386	tggaggctcgagcggtggcggccgcatggtgaggtggtttcaccgggacc	Clone mouse SHP1 into pMIG II-mCherry vector	pMIG II-mCherry-mouse SHP1
EH-1387	tggaggctcgagcggtggcggccgcatgacatcgcggagatgg		
EH-1389	cgactctagagtcgcggccgctcacttcctcttgagagaacctttg	Clone mouse SHP2 into pMIG II-mCherry vector	pMIG II-mCherry-mouse SHP2
EH-1390	cgactctagagtcgcggccgctcatctgaaactcctctgctg		
EH-899	caccgtcggcccagtcgcaagaacc	SHP1_gRNA1	pX330-GFP SHP1_gRNA1
EH-900	aaacggttcttgcgactgggccga		
EH-901	caccggacacctcggcccttgagc	SHP1_gRNA2	pX330-GFP SHP1_gRNA2
EH-902	aaacgctcaagggccgaggtgtc		
EH-387	caccggagacttcacactttccgtt	SHP2_gRNA1	pX330-GFP SHP2_gRNA1
EH-388	aaacaacggaaagtgtgaagtctcc		
EH-389	caccgtacagtactacaactcaagc	SHP2_gRNA2	pX330-GFP SHP2_gRNA2
EH-390	aaacgcttgagttgtagtactgtac		
EH-26	tggacagcaaatgggtcgcggacgggccgcacgaggga	Clone human PD-1^{INT} into pET28A-His10 vector	pET28A-His$_{10}$–PD-1^{INT}
EH-1949	gagctcgaattcgtcacaggggccaagagc		
EH-1498	cagcaaatgggtcgcggaggcttctgggaggagttt	Clone human SHP1^{PTPase} into pET28A-His$_{10}$ vector	pET28A-His$_{10}$-SHP1^{PTPase}
EH-1499	gacggagctcgaattcttaataggtgatgttcccgtact		

Xu et al.
Comparative analysis of PD-1 and BTLA signaling

Journal of Cell Biology 14 of 20
https://doi.org/10.1083/jcb.201905085

Table 1. **List of oligos** (*Continued*)

Name	Sequence (5'- to -3')	Purpose	Construct
EH-1502	ggacagcaaatgggtcgcggatccggcttttgggaggaatttg	Clone human SHP2^{PTPase} into pET28A-His$_{10}$ vector	pET28aA-His$_{10}$-SHP2^{PTPase}
EH-1538	gtcgacggagctcgaattctcaatacttaatatttgtatattcgtgcc		
EH-606	ctttaagaaggagatataccatgggcagcagccatcat	Clone His$_{10}$-human BTLA^{INT} (WT, YFFF, FYFF, FFYF, or FFFY) into pET28A-TwinStrep vector	pET28A-His$_{10}$-BTLA^{INT} (WT, YFFF, FYFF, FFYF or FFFY)_TwinStrep
EH-607	tccacctttctcgaactgcgggtggctccaggatccactcctcacacatatgg		

Scientific; #88223) and eluted with Hepes buffered saline (HBS; 50 mM Hepes-NaOH, pH 7.5, and 150 mM NaCl) containing 500 mM imidazole (Sigma-Aldrich; #I202). BTLA^{INT} (aa 190–289), BTLA$^{INT/YFFF}$ mutant (aa 190–289, Y243F, Y257F, Y282F), BTLA$^{INT/FYFF}$ mutant (aa 190–289, Y226F, Y257F, 282F), BTLA$^{INT/FFYF}$ mutant (aa 190–289, Y226F, Y243F, Y282F), and BTLA$^{INT/FFFY}$ mutant (aa 190–289, Y226F, Y243F, Y257F) were expressed with an N-terminal His$_{10}$ tag and a C-terminal TwinStrep tag in *E. coli* using the pET28A vector, purified using a StrepTrap HP Column (GE Healthcare; #95056–056), and eluted with HBS buffer containing 1 mM d-Desthiobiotin (Sigma-Aldrich; #D1411-1G).

For GST pull-down assays, human PD-1^{INT} (aa 194–288) and PD-1$^{INT/FF}$ mutant (aa 194–288, Y223F, Y248F) were expressed with an N-terminal GST tag in *E. coli* using the pGEX-6p2 vector, purified using Glutathione Sepharose 4B (GoldBio; #G-250), and eluted with HBS buffer containing 10 mM reduced glutathione (Sigma-Aldrich; #G4251) to obtain soluble GST-tagged proteins. BTLA^{INT} (aa 190–289) and BTLA$^{INT/FFFF}$ mutant (aa 190–289, Y226F, Y243F, Y257F, Y282F) were expressed with an N-terminal GST tag and a C-terminal TwinStrep tag in *E. coli* using the pET28A vector, purified using a StrepTrap HP Column, and eluted with HBS buffer containing 1 mM d-Desthiobiotin.

For FRET assays, P50 and ZAP70^{tSH2} proteins were expressed with an N-terminal GST tag followed by a PreScission recognition sequence (LEVLFQGP) and a SNAP-tag in *E. coli* using the pGEX6p-2 vector. Recombinant SHP1 and SHP2 proteins were expressed with an N-terminal GST tag followed by a PreScission recognition sequence (LEVLFQGP) and a SNAP-tag using the Bac-to-Bac baculovirus system. Proteins were purified using Glutathione Sepharose 4B and eluted with HBS buffer containing 20 U/ml 3C protease to remove the GST tag.

All affinity purified proteins were subjected to gel filtration chromatography using HBS buffer containing 10% glycerol and 1 mM TCEP. The monomer fractions were pooled, snap frozen, and stored at –80°C in small aliquots.

Cell line generation
To generate SHP2 KO Raji cells and SHP1 KO or SHP2 KO Jurkat cells, two different sgRNAs specific for *PTPN6* (*SHP1*) or *PTPN11* (*SHP2*) encoded in the PX330-GFP vectors were electroporated into Raji or Jurkat cells using a Gene Pulser Xcell (Bio-Rad) following a built-in exponential protocol (250 V; 1,000 μF; ∞ Ω; and 4-mm cuvette). After electroporation, cells were recovered in culture medium for 2 d at 37°C/5% CO$_2$. Single GFP-positive cells were then sorted to a 96-well plate with FACSAria Fusion (BD Biosciences) and maintained in culture media for 3 wk, after

which the corresponding KO cell clones were validated by Western blot with mouse anti-human SHP1 antibody or mouse anti-human SHP2 antibody. To generate SHP1 and SHP2 double KO Jurkat cells, two different sgRNAs specific for *PTPN6* (*SHP1*) encoded in the PX330-GFP vector were electroporated into SHP2 KO Jurkat cells, and the double KO clones were sorted and validated using the foregoing methods.

Each gene of interest was introduced into Jurkat and Raji cells via lentiviral transduction, as described previously (Zhao et al., 2018). Briefly, each cDNA was cloned into a pHR backbone vector, and cotransfected with pMD2.G and psPAX2 packaging plasmids into HEK293T cells using polyethylenimine (Thermo Fisher Scientific; #NC1014320). Lentiviruses were harvested at 60–72 h after transfection. Jurkat and Raji cells were spin-infected at 35°C, 1,000× g for 30 min, and incubated at 37°C/5% CO$_2$ overnight. Raji (PD-L1–mCherry$^+$) and Raji (HVEM-mRuby$^+$) cells were generated by transducing *PD-L1–mCherry* or *HVEM-mRuby* to WT Raji cells. SHP2 KO Raji (PD-L1–mCherry$^+$) and SHP2 KO Raji (HVEM-mRuby$^+$) cells were generated by transducing *PD-L1–mCherry* or *HVEM-mRuby* into SHP2 KO Raji cells. Analogously, WT Jurkat, SHP1 KO Jurkat, SHP2 KO Jurkat, or SHP1/2 DKO Jurkat cells were transduced with *PD-1^{FF}–mGFP*, *PD-1^{WT}–mGFP*, *BTLA^{FFFF}–mGFP*, or *BTLA^{WT}–mGFP* to generate Jurkat lines stably expressing the corresponding PD-1 or BTLA fusion proteins. Jurkat (PD-1$^{ECTO-TMD}$–BTLA^{INT}–mGFP$^+$) cells were generated by transducing WT Jurkat cells with a pHR plasmid encoding the fusion gene. All the above fusion genes were driven by the SFFV promoter. Jurkat (BTLA$^{ECTO-TMD}$–PD-1^{INT}–mGFP$^+$) cells were generated by transducing WT Jurkat cells with a pHR plasmid encoding the fusion gene under the control of the dSV40 promoter.

Jurkat-Raji co-culture assay
For Fig. 1, E and F; Fig. 2 B; Fig. 3, A and B; Fig. 4, C and F; Fig. 6, C–E; and Fig. S4, Jurkat cells were starved in serum-free RPMI medium at 37°C for 3 h before conjugation to reduce the phosphorylation background. Raji B cells were preincubated with 30 ng/ml SEE in RPMI medium for 30 min at 37°C. Afterward, 2 × 10^6 SEE-loaded Raji B cells and 2 × 10^6 Jurkat T cells were precooled on ice and mixed in a 96-well plate. The plate was then centrifuged at 300× g for 1 min at 4°C to initiate cell–cell contact and immediately transferred to a 37°C water bath. The reactions were terminated with lysis buffer (50 mM Hepes-NaOH, pH 7.4, 150 mM NaCl, 1% NP-40, 5% glycerol, 1 mM EDTA, 1 mM PMSF, 10 mM Na$_3$VO$_4$, and 10 mM NaF) at indicated time points. CD28 was immunoprecipitated from the lysates using protein G Dynabeads coupled with an anti-CD28 antibody. BTLA^{WT}-mGFP

Xu et al.
Comparative analysis of PD-1 and BTLA signaling

Journal of Cell Biology 15 of 20
https://doi.org/10.1083/jcb.201905085

and PD-1^{WT}–mGFP were immunoprecipitated from the lysate using GFP-Trap. Equal fractions of the IP samples were subjected to SDS-PAGE and immunoblotted with indicated antibodies.

For the IL-2 data shown in Fig. 1, B and D; Fig. 6, F–H; Fig. S3, and Table S1, Raji B cells were preincubated with 30 ng/ml SEE in RPMI medium for 30 min at 37°C. Afterward, 10^5 SEE-loaded Raji B cells and 2×10^5 serum-starved Jurkat T cells were mixed in a 96-well U-bottom plate in triplicate wells. The plate was then centrifuged at 300× g for 1 min to initiate cell–cell contact and immediately transferred to a 37°C/5% CO_2 incubator. Supernatants were collected at 6 h after stimulation. IL-2 levels were quantified by an ELISA kit (BioLegend; #431804). We have noted that IL-2 production depended on the age of the cells; therefore, to minimize the uncertainties, we conducted all IL-2 assays in at least six independent replicates on at least six consecutive days, so that different Jurkat lines were compared at the same age range. On each day, IL-2 ELISA was run in three technical replicates per Jurkat line, and the mean IL-2 level for each line was normalized to that of the Jurkat (PD-1^{FF}–mGFP⁺) line or to that of the Jurkat (BTLA^{FFFF}-mGFP⁺) line under the same SHP background.

Flow cytometry

Flow cytometry was performed using either an LSRFortessa cell analyzer (BD Biosciences) or a FACSAria Fusion cell sorter (BD Biosciences), and data were analyzed using FlowJo (FlowJo, LLC). For Fig. 1, A and C; Fig. 4, B and E; Fig. 6 B; and Fig. S1, A and B, Jurkat cells were stained with anti-BTLA PE, anti–PD-1 PE, or anti-CD28 Allophycocyanin to detect BTLA, PD-1, or CD28 expression, respectively. For Fig. S1 D, Raji cells were stained with anti-HVEM Allophycocyanin or anti–PD-L1 Allophycocyanin to detect HVEM or PD-L1 expression. For proliferation assays in Fig. 7, C and F; and Fig. S5, A and D, mouse CD8⁺ T cells were stained with CTV dye and subjected to flow cytometry. For Fig. 7, B, D, E, G, and H; and Fig. S5, B, C, E, and F, PD-1, IL-2, or IFN-γ⁺ cells were stained with anti-mouse PD-1 FITC, anti-mouse IL-2 FITC, or anti-mouse IFN-γ PE, respectively.

GST pull down

For Fig. 2 A, soluble GST-tagged baits (PD-1^{INT} or BTLA^{INT}, 10 µg) were prephosphorylated by 0.2 µg His₁₀-Lck^{G2A} at RT in the presence of 1 mM ATP for 1 h and then mixed with the cleared cell lysate of 3×10^7 Jurkat cells prestimulated by 1.5×10^7 SEE-pulsed Raji cells. After 3-h incubation at 4°C, during which the baits bound to proteins in the lysate, 100 µl glutathione agarose resin was added and rotated for 1 h at 4°C. Resin was then rinsed four times with 1 ml wash buffer (20 mM Hepes-NaOH, pH 7.4, 50 mM NaCl, 0.1% NP-40, 1 mM EDTA, 10 mM Na₃VO₄, and 10 mM NaF), and proteins were eluted by 1 × SDS sample buffer at 95°C for 10 min.

Sample processing for MS

The samples were in-gel digested as described previously (Gendron et al., 2016; Peled et al., 2018). Briefly, the gel pieces of the samples to be analyzed were reduced with 10 mM DTT (Acros Organics; #16568-0050) for 30 min at 56°C and then

alkylated with 50 mM iodoacetamide (MP Biomedicals; #100351) for 30 min at RT protected from light, digested with sequencing grade modified Trypsin (Promega; #V511A) at a ratio of 1:100 (enzyme:substrate) in 50 mM ammonium bicarbonate (Sigma-Aldrich; #5330050050) buffer, and incubated overnight at 37°C. The trypsin digested supernatant was transferred to a 1.5-ml Eppendorf tube. Peptides were extracted from the gel pieces by adding 10% formic acid and 100% acetonitrile (ACN) sequentially before transfer to the previous supernatant and were dried using a speed vac (Eppendorf). The dried peptides were resuspended in 10 µl of peptide reconstitution solution (5% ACN/5% formic acid) and transferred to autosampler vials for MS analysis.

Nano liquid chromatography-tandem mass spectrometry (nLC-MS/MS)

Samples were analyzed in duplicate by nLC-MS/MS using a Q-Exactive mass spectrometer (Thermo Fisher Scientific) coupled with an EASY-nLC 1000 (Thermo Fisher Scientific) chromatography system. Peptides were first separated by reverse-phase chromatography using a fused silica microcapillary column (75-µm inner diameter, 15 cm) packed with C18 reverse-phase resin (ReproSil-pur 120 C18-AQ, 1.9 µm; Dr. Maisch GmbH) using an in-line nano-flow EASY-nLC 1000 UHPLC. Peptides were eluted over a 100-min 2%–30% ACN gradient, a 5-min 30%–60% ACN gradient, and a 5-min 60%–95% ACN gradient, with a final 10-min step at 0% ACN for a total run time of 120 min at a flow rate of 250 nl/min. All gradient mobile phases contained 0.1% formic acid. MS/MS data were collected in a data-dependent fashion using a top 10 method with a full MS mass range from 400 to 1,800 m/z, 70,000 resolution, and an automatic gain control target of 3e6. MS2 scans were triggered when an ion intensity threshold of 1e5 was reached with a maximum injection time of 60 ms. Peptides were fragmented using a normalized collision energy setting of 25. A dynamic exclusion time of 40 s was used, and the peptide match setting was disabled. Singly charged ions, charge states >8, and unassigned charge states were excluded. The MS/MS spectra were searched against the UniProt Human reference proteome database (downloaded June 2, 2018) integrated with WT and signaling-deficient mutant of GST–PD-1^{INT} (aa 194–288) and GST-BTLA^{INT} (aa 190–289) sequences, using SEQUEST in Proteome Discoverer (Thermo Fisher Scientific) with 1% false discovery rate. Identified proteins were further quantified through the abundance of their unique peptides using Proteome Discoverer. Database queries from UniProt were used to sort for SH2-containing proteins.

FRET assays with protein-reconstituted LUVs

LUVs consisting of 89.7% POPC, 10% DGS-NTA-Ni, and 0.3% Rhod-PE were generated by extrusion as described (Hui and Vale, 2014). Briefly, desired lipids were mixed in chloroform, dried under a nitrogen stream, and desiccated in a vacuum container for 1 h. Subsequently, lipid film was resuspended in 1× kinase buffer (50 mM Hepes-NaOH, pH 7.4, 150 mM NaCl, and 10 mM MgCl₂) and extruded 20 times through a pair of polycarbonate filters containing pores of 200-nm diameter. For Fig. 5, A and C, 2.76 nM LUVs in 1× kinase buffer supplemented with 0.5 mg/ml BSA and 1 mM TCEP were incubated with 5 nM

His$_{10}$-Lck^{G2A}, 300 nM His$_{10}$-CD3ζ^{INT} or His$_{10}$-CD28^{INT}, 100 nM SC505*ZAP70^{tSH2} or SC505*P50, and increasing levels of His$_{10}$-SHP1^{PTPase} or His$_{10}$-SHP2^{PTPase} in a 96-well solid white microplate (Greiner Bio-One; #655075), during which the SC505 fluorescence was monitored in real time using a plate reader (Tecan Spark 20) with 504-nm excitation and 540-nm emission. Following 40-min incubation, ATP was injected to a final concentration of 1 mM and SC505 fluorescence monitored for an additional 1 h. Fig. 5 E was set up as the 50-nM SHP^{PTPase} conditions in Fig. 5 A except with the addition of 0.5 U apyrase at 30 min after ATP injection. For Fig. 5 F, His$_{10}$-SHP1^{PTPase} or His$_{10}$-SHP2^{PTPase} in Fig. 5 A was replaced with non–His-tagged SNAP-SHP1 or non–His-tagged SNAP-SHP2 and increasing levels of His$_{10}$-BTLA^{INT}. For Fig. 5 G, His$_{10}$-BTLA^{INT} in Fig. 5 F was replaced with equal concentrations of His$_{10}$–PD-1^{INT}. Data were normalized by the mean fluorescence intensity of the last 10 data points before the addition of ATP and plotted with GraphPad Prism 5.0. All experiments described in this section were conducted at room temperature.

OT-1: PLB imaging assay

OT-1 primary T cells were retrovirally transduced with either *Pd-1–mGFP* plus *mCherry-Shp1*, *Pd-1–mGFP* plus *mCherry-Shp2*, *Btla-mGFP* plus *mCherry-Shp1*, or *Btla-mGFP* plus *mCherry-Shp2*. To produce retroviruses, each cDNA was cloned into the pMSCV vector and cotransfected with pCl-Eco packaging plasmid into Phoenix-Eco retrovirus packaging cell line using polyethylenimine. Virus supernatants were harvested at 48 and 72 h after transfection. Freshly harvested OT-1 splenocytes were stimulated with 10 nM SIINFEKL peptide (Anaspec; #AS-60193-1) in RPMI medium supplemented with 10% FBS, 100 U/ml of recombinant mouse IL-2, 100 U/ml of penicillin, and 100 µg/ml of streptomycin, 50 µM β-ME at 37°C/5% CO$_2$. 36 h later, cells were resuspended in retrovirus supernatants containing 8 mg/ml Lipofectamine and 100 U/ml recombinant mouse IL-2, spin-infected at 35°C, 1,000× *g* for 120 min, and incubated at 37°C/5% CO$_2$ overnight. The virus supernatant was replaced with fresh OT-1 culture medium supplemented with 10 nM SIINFEKL peptide, 100 U/ml recombinant mouse IL-2, and 50 µM β-ME the second day, and cells were incubated for another 48–96 h before microscopy. To form PLB, a glass-bottom 96-well plate was incubated with 5% Hellmanex III (Hëlma Analytics; #Z805939) overnight on a 50°C heat pad, thoroughly rinsed with ddH2O, and sealed with Nunc sealing tape (Thermo Fisher Scientific; #232698). The desired wells were washed twice with 5 M NaOH and three times with 500 ml ddH2O followed by equilibration with PBS.

SUVs (consisting of 97.5% POPC, 2% DGS-NTA-Ni, and 0.5% PEG5000-PE) were prepared as described previously (Hui et al., 2017). Briefly, desired lipids were mixed in chloroform, dried under a nitrogen stream, and desiccated in a vacuum container for 1 h and suspended in PBS. SUVs were formed via 20 freeze-thaw cycles of the lipid suspension, which were then centrifuged at 33,500× *g* for 45 min at 4°C using a TLA120 rotor (Beckman Coulter) to remove multilamellar vesicles. Supernatant containing SUVs was collected and added to the cleaned wells containing 200 µl PBS and incubated for 90 min at 50°C,

followed by 30 min at 37°C to induce PLB formation. The PLBs were then rinsed thoroughly with PBS to remove excess SUVs and incubated in PBS for 30 min at 37°C. For Fig. 2 D, PLB was functionalized by a mixture of 5 nM pMHC-I-His, 2 nM mouse ICAM-His (Sino Biological; #50440-M08H), 3 nM mouse CD86-His (Sino Biological; #50068-M08H), and either 8 nM mouse PD-L1–His (Sino Biological; #50010-M08H) or 8 nM mouse HVEM-His (BioLegend; #771304). Transduced OT-1 cells were harvested via centrifugation at 200× *g* for 4 min and incubated with 10 µg/ml AF647-labeled mouse TCRβ antibody (BioLegend; #H57-597) for 30 min on ice. Both PLBs and stained OT-1 cells were washed twice with PBS and once with imaging buffer (20 mM Hepes-NaOH, pH 7.5, 137 mM NaCl, 5 mM KCl, 1 mM CaCl$_2$, 2 mM MgCl$_2$, 0.7 mM Na$_2$HPO$_4$, and 6 mM D-glucose). Then cells were overlaid onto functionalized PLBs for 10 min at 37°C before fixing with 4% PFA in PBS for another 10 min. TIRF images were acquired at RT on a Nikon Eclipse Ti microscope equipped with a 100× Apo TIRF 1.49 NA objective and an Andor iXon Ultra 897 electron multiplying charge-coupled device camera controlled by Micro-Manager software (Edelstein et al., 2014) and analyzed with ImageJ. PCCs for PD-1–mGFP/mCherry-SHP1, PD-1–mGFP/mCherry-SHP2, BTLA-mGFP/mCherry-SHP1, and BTLA-mGFP/mCherry-SHP2 were calculated using the "Colocalization test" tool in ImageJ after subtracting background of each channel of the entire cell.

Jurkat:PLB imaging assay

PLBs were prepared as described above. For Fig. 3 C and Video 1, PLBs were incubated with a mixture of 75 nM His-protein G, 3 nM human ICAM-1-His (Sino Biological; #10346-H08H), and 0.5 nM of human PD-L1–His (Sino Biological; #10084-H08H) for 1 h at 37°C. After incubation, PLBs were washed with PBS to remove unbound His-tagged proteins and further incubated with 4 µg/ml Alexa647–anti-CD3ε (OKT3 clone; BioLegend; #317312) for 30 min at 37°C. PLBs were washed twice with PBS and once with imaging buffer. 2 × 10^5 SHP1/2 DKO Jurkat (PD-1–mGFP$^+$, mCherry-SHP1$^+$) cells or SHP1/2 DKO Jurkat (PD-1–mGFP$^+$, mCherry-SHP2$^+$) cells were harvested via centrifugation at 200× *g* for 4 min, resuspended in imaging buffer, and overlaid to the PLBs for TIRF imaging. Image acquisitions and colocalization indices were measured as described above.

Dynabead coating for CD8$^+$ T cell stimulation

Protein G Dynabeads were washed twice by PBS before coating with proteins or antibodies. For the "IgG alone" group, 3 × 10^8 Dynabeads were mixed with 20 µg mouse IgG; for the "anti-CD3/anti-CD28+IgG" group, the same number of Dynabeads was mixed with 1 µg purified anti-mouse CD3, 2 µg purified anti-mouse CD28, and 17 µg mouse IgG; for the "anti-CD3/anti-CD28/PD-L1^{Lo} or HVEM^{Lo}" group, 1 µg purified anti-mouse CD3, 2 µg purified anti-mouse CD28, 3.4 µg mouse PD-L1-Fc or mouse HVEM-Fc, and 13.4 µg mouse IgG were mixed with Dynabeads; for the "anti-CD3/anti-CD28/PD-L1^{Hi} or HVEM^{Hi}" group, 1 µg purified anti-mouse CD3, 2 µg purified anti-mouse CD28, and 17 µg mouse PD-L1-Fc or mouse HVEM-Fc were mixed with Dynabeads. The mixtures were incubated at RT for 30 min with vortexing every 5 min. Unbound antibodies or proteins were

removed by two washes with PBS, and coated Dynabeads were resuspended in PBS.

In vitro stimulation of naive CD8^{+} T cells

For Fig. 7 and Fig. S5, *Ptpn6*^{fl/fl};*Ptpn11*^{fl/fl} (WT) mice or *dLck-Cre*; *Ptpn6*^{fl/fl};*Ptpn11*^{fl/fl} (SHP1/2 DKO) mice were euthanatized by CO_2. Spleens and all lymph nodes were collected and gently ground using a syringe and a homemade iron mesh to produce single-cell suspensions. Erythrocytes were lysed by a homemade ACK buffer (155 mM NH_4Cl, 10 mM $KHCO_3$, and 0.1 mM EDTA), and total splenocytes and lymphocytes were stained with anti-mouse CD4 biotin, anti-mouse CD44 biotin, anti-mouse CD45RA/B220 biotin, anti-mouse CD25 biotin, anti-mouse NK1.1 biotin, anti-mouse CD11b biotin, and anti-mouse CD11c biotin antibodies; stained cells were then removed with BeaverBeads Streptavidin. The remaining cells were stained with anti-mouse CD8 Allophycocyanin-eFluor 780 and anti-mouse CD44 eFluor 450 before sorting out naive CD8^{+} T cells using a FACSAria Fusion flow cytometer (BD Biosciences). Purities of naive CD8^{+} T cells used for in vitro stimulation were higher than 95%. Naive CD8^{+} T cells were labeled with 1 mM CTV for 15 min at 37°C. Upon removal of free dyes by PBS washes, labeled cells were resuspended to a density of 10^6 cells/ml in RPMI-1640 medium containing 10% FBS, 100 U/ml recombinant mouse IL-2, 50 μM β-ME, 100 U/ml of penicillin, and 100 μg/ml of streptomycin. Subsequently, protein-coated Dynabeads were added into the cell suspension to reach a 4.5:1 beads-to-cells ratio and incubated at 37°C/5% CO_2. Cells were collected at 24, 48, and 72 h for further analyses. For surface molecule analysis, cells were stained using anti-mouse CD8 Allophycocyanin-eFluor 780, anti-mouse CD44 Allophycocyanin, or anti-mouse PD-1 FITC for 20 min at 4°C, and data were collected using the LSRFortessa cell analyzer. For intracellular cytokine analysis, cells were first restimulated using 50 ng/ml PMA, 1 μg/ml ionomycin, and BD GolgiStop Protein Transport Inhibitor (1:1,500) in RPMI-1640 medium for 4 h at 37°C, and treated with the Fixation/Permeabilization Solution Kit. Cytokines were stained with anti-mouse IFN-γ PE and anti-mouse IL-2 FITC, and data were collected with the foregoing analyzer.

Quantification and statistical analysis

Data are shown as mean ± SD, and the number of replicates is indicated in the figure legends. Curve fitting and normalization were performed in GraphPad Prism 5. Data distribution was assumed to be normal, but this was not formally tested. Statistical significance was evaluated by two-way ANOVA or Student's *t* test (*, $P < 0.05$; **, $P < 0.01$; ***, $P < 0.001$; ****, $P < 0.0001$; ns, not significant). Data with $P < 0.05$ are considered statistically significant.

Online supplemental material

Fig. S1 shows the expression levels of PD-1, BTLA, CD28, PD-L1, or HVEM in different Jurkat cells or Raji cells. Fig. S2 shows that anti-pY antibody pY20 prefers pY227 and pY243 on BTLA[INT]. Fig. S3 shows the raw and normalized IL-2 levels of Jurkat E6.1 cells from two independent sources. Fig. S4 shows phosphorylation of PD-1 or BTLA in SHP1 KO Jurkat cells or SHP1/2 DKO

Jurkat cells. Fig. S5 shows that HVEM inhibits the functions of WT and SHP1/2 DKO CD8^{+} T cells. Video 1 is a time-lapse TIRF movie of a PLB-interacting Jurkat cell showing PD-1 recruitment of SHP2 but not SHP1. Table S1 summarizes the percentage of IL-2 inhibition by PD-1 or BTLA in WT, SHP1 KO, SHP2 KO, and SHP1/2 DKO Jurkat cells.

Acknowledgments

References

Ahrends, T., A. Spanjaard, B. Pilzecker, N. Bąbała, A. Bovens, Y. Xiao, H. Jacobs, and J. Borst. 2017. CD4^{+} T Cell Help Confers a Cytotoxic T Cell Effector Program Including Coinhibitory Receptor Downregulation and Increased Tissue Invasiveness. *Immunity*. 47:848–861.e5. https://doi .org/10.1016/j.immuni.2017.10.009

Baitsch, L., P. Baumgaertner, E. Devêvre, S.K. Raghav, A. Legat, L. Barba, S. Wieckowski, H. Bouzourene, B. Deplancke, P. Romero, et al. 2011. Exhaustion of tumor-specific CD8^{+} T cells in metastases from melanoma patients. *J. Clin. Invest.* 121:2350–2360. https://doi.org/10.1172/JCI46102

Baitsch, L., A. Legat, L. Barba, S.A. Fuertes Marraco, J.P. Rivals, P. Baumgaertner, C. Christiansen-Jucht, H. Bouzourene, D. Rimoldi, H. Pircher, et al. 2012. Extended co-expression of inhibitory receptors by human CD8 T-cells depending on differentiation, antigen-specificity and anatomical localization. *PLoS One.* 7. e30852. https://doi.org/10.1371/journal .pone.0030852

Cai, G., A. Anumanthan, J.A. Brown, E.A. Greenfield, B. Zhu, and G.J. Freeman. 2008. CD160 inhibits activation of human CD4+ T cells through interaction with herpesvirus entry mediator. *Nat. Immunol.* 9:176–185. https://doi.org/10.1038/ni1554

Carreno, B.M., and M. Collins. 2003. BTLA: a new inhibitory receptor with a B7-like ligand. *Trends Immunol.* 24:524–527. https://doi.org/10.1016/j.it .2003.08.005

Celis-Gutierrez, J., P. Blattmann, Y. Zhai, N. Jarmuzynski, K. Ruminski, C. Grégoire, Y. Ounoughene, F. Fiore, R. Aebersold, R. Roncagalli, et al. 2019. Quantitative Interactomics in Primary T Cells Provides a Rationale for Concomitant PD-1 and BTLA Coinhibitor Blockade in Cancer Immunotherapy. *Cell Rep*. 27:3315–3330.e7. https://doi.org/10.1016/j.celrep.2019.05.041

Chemnitz, J.M., R.V. Parry, K.E. Nichols, C.H. June, and J.L. Riley. 2004. SHP-1 and SHP-2 associate with immunoreceptor tyrosine-based switch motif of programmed death 1 upon primary human T cell stimulation, but only receptor ligation prevents T cell activation. *J. Immunol*. 173: 945–954. https://doi.org/10.4049/jimmunol.173.2.945

Chemnitz, J.M., A.R. Lanfranco, I. Braunstein, and J.L. Riley. 2006. B and T lymphocyte attenuator-mediated signal transduction provides a potent inhibitory signal to primary human CD4 T cells that can be initiated by multiple phosphotyrosine motifs. *J. Immunol*. 176:6603–6614. https://doi.org/10.4049/jimmunol.176.11.6603

Chen, L., and D.B. Flies. 2013. Molecular mechanisms of T cell co-stimulation and co-inhibition. *Nat. Rev. Immunol*. 13:227–242. https://doi.org/10.1038/nri3405

Cheng, X., V. Veverka, A. Radhakrishnan, L.C. Waters, F.W. Muskett, S.H. Morgan, J. Huo, C. Yu, E.J. Evans, A.J. Leslie, et al. 2013. Structure and interactions of the human programmed cell death 1 receptor. *J. Biol. Chem*. 288:11771–11785. https://doi.org/10.1074/jbc.M112.448126

Cheung, T.C., L.M. Oborne, M.W. Steinberg, M.G. Macauley, S. Fukuyama, H. Sanjo, C. D'Souza, P.S. Norris, K. Pfeffer, K.M. Murphy, et al. 2009. T cell intrinsic heterodimeric complexes between HVEM and BTLA determine receptivity to the surrounding microenvironment. *J. Immunol*. 183:7286–7296. https://doi.org/10.4049/jimmunol.0902490

Choi, Y.W., B. Kotzin, L. Herron, J. Callahan, P. Marrack, and J. Kappler. 1989. Interaction of Staphylococcus aureus toxin "superantigens" with human T cells. *Proc. Natl. Acad. Sci. USA*. 86:8941–8945. https://doi.org/10.1073/pnas.86.22.8941

Compaan, D.M., L.C. Gonzalez, I. Tom, K.M. Loyet, D. Eaton, and S.G. Hymowitz. 2005. Attenuating lymphocyte activity: the crystal structure of the BTLA-HVEM complex. *J. Biol. Chem*. 280:39553–39561. https://doi.org/10.1074/jbc.M507629200

Croft, M.. 2003. Co-stimulatory members of the TNFR family: keys to effective T-cell immunity? *Nat. Rev. Immunol*. 3:609–620. https://doi.org/10.1038/nri1148

Derré, L., J.P. Rivals, C. Jandus, S. Pastor, D. Rimoldi, P. Romero, O. Michielin, D. Olive, and D.E. Speiser. 2010. BTLA mediates inhibition of human tumor-specific CD8+ T cells that can be partially reversed by vaccination. *J. Clin. Invest*. 120:157–167. https://doi.org/10.1172/JCI40070

Edelstein, A.D., M.A. Tsuchida, N. Amodaj, H. Pinkard, R.D. Vale, and N. Stuurman. 2014. Advanced methods of microscope control using µManager software. *J. Biol. Methods*. 1. e10. https://doi.org/10.14440/jbm.2014.36

Fourcade, J., Z. Sun, O. Pagliano, P. Guillaume, I.F. Luescher, C. Sander, J.M. Kirkwood, D. Olive, V. Kuchroo, and H.M. Zarour. 2012. CD8(+) T cells specific for tumor antigens can be rendered dysfunctional by the tumor microenvironment through upregulation of the inhibitory receptors BTLA and PD-1. *Cancer Res*. 72:887–896. https://doi.org/10.1158/0008-5472.CAN-11-2637

Freeman, G.J., A.J. Long, Y. Iwai, K. Bourque, T. Chernova, H. Nishimura, L.J. Fitz, N. Malenkovich, T. Okazaki, M.C. Byrne, et al. 2000. Engagement of the PD-1 immunoinhibitory receptor by a novel B7 family member leads to negative regulation of lymphocyte activation. *J. Exp. Med*. 192: 1027–1034. https://doi.org/10.1084/jem.192.7.1027

Fuertes Marraco, S.A., N.J. Neubert, G. Verdeil, and D.E. Speiser. 2015. Inhibitory receptors beyond T cell exhaustion. *Front. Immunol*. 6:310. https://doi.org/10.3389/fimmu.2015.00310

Gavrieli, M., and K.M. Murphy. 2006. Association of Grb-2 and PI3K p85 with phosphotyrosile peptides derived from BTLA. *Biochem. Biophys. Res. Commun*. 345:1440–1445. https://doi.org/10.1016/j.bbrc.2006.05.036

Gavrieli, M., N. Watanabe, S.K. Loftin, T.L. Murphy, and K.M. Murphy. 2003. Characterization of phosphotyrosine binding motifs in the cytoplasmic domain of B and T lymphocyte attenuator required for association with protein tyrosine phosphatases SHP-1 and SHP-2. *Biochem. Biophys. Res. Commun*. 312:1236–1243. https://doi.org/10.1016/j.bbrc.2003.11.070

Gendron, J.M., K. Webb, B. Yang, L. Rising, N. Zuzow, and E.J. Bennett. 2016. Using the Ubiquitin-modified Proteome to Monitor Distinct and Spatially Restricted Protein Homeostasis Dysfunction. *Mol. Cell. Proteomics*. 15:2576–2593. https://doi.org/10.1074/mcp.M116.058420

Gonzalez, L.C., K.M. Loyet, J. Calemine-Fenaux, V. Chauhan, B. Wranik, W. Ouyang, and D.L. Eaton. 2005. A coreceptor interaction between the CD28 and TNF receptor family members B and T lymphocyte attenuator and herpesvirus entry mediator. *Proc. Natl. Acad. Sci. USA*. 102:1116–1121. https://doi.org/10.1073/pnas.0409071102

Goyette, J., C.S. Salas, N. Coker-Gordon, M. Bridge, S.A. Isaacson, J. Allard, and O. Dushek. 2017. Biophysical assay for tethered signaling reactions reveals tether-controlled activity for the phosphatase SHP-1. *Sci. Adv*. 3. e1601692. https://doi.org/10.1126/sciadv.1601692

Grabmeier-Pfistershammer, K., C. Stecher, M. Zettl, S. Rosskopf, A. Rieger, G.J. Zlabinger, and P. Steinberger. 2017. Antibodies targeting BTLA or TIM-3 enhance HIV-1 specific T cell responses in combination with PD-1 blockade. *Clin. Immunol*. 183:167–173. https://doi.org/10.1016/j.clim.2017.09.002

Hamid, O., C. Robert, A. Daud, F.S. Hodi, W.J. Hwu, R. Kefford, J.D. Wolchok, P. Hersey, R.W. Joseph, J.S. Weber, et al. 2013. Safety and tumor responses with lambrolizumab (anti-PD-1) in melanoma. *N. Engl. J. Med*. 369:134–144. https://doi.org/10.1056/NEJMoa1305133

Herbst, R.S., J.C. Soria, M. Kowanetz, G.D. Fine, O. Hamid, M.S. Gordon, J.A. Sosman, D.F. McDermott, J.D. Powderly, S.N. Gettinger, et al. 2014. Predictive correlates of response to the anti-PD-L1 antibody MPDL3280A in cancer patients. *Nature*. 515:563–567. https://doi.org/10.1038/nature14011

Hui, E., and R.D. Vale. 2014. In vitro membrane reconstitution of the T-cell receptor proximal signaling network. *Nat. Struct. Mol. Biol*. 21:133–142. https://doi.org/10.1038/nsmb.2762

Hui, E., J. Cheung, J. Zhu, X. Su, M.J. Taylor, H.A. Wallweber, D.K. Sasmal, J. Huang, J.M. Kim, I. Mellman, et al. 2017. T cell costimulatory receptor CD28 is a primary target for PD-1-mediated inhibition. *Science*. 355: 1428–1433. https://doi.org/10.1126/science.aaf1292

Hukelmann, J.L., K.E. Anderson, L.V. Sinclair, K.M. Grzes, A.B. Murillo, P.T. Hawkins, L.R. Stephens, A.I. Lamond, and D.A. Cantrell. 2016. The cytotoxic T cell proteome and its shaping by the kinase mTOR. *Nat. Immunol*. 17:104–112. https://doi.org/10.1038/ni.3314

Hurchla, M.A., J.R. Sedy, M. Gavrieli, C.G. Drake, T.L. Murphy, and K.M. Murphy. 2005. B and T lymphocyte attenuator exhibits structural and expression polymorphisms and is highly Induced in anergic CD4+ T cells. *J. Immunol*. 174:3377–3385. https://doi.org/10.4049/jimmunol.174.6.3377

Iwai, Y., J. Hamanishi, K. Chamoto, and T. Honjo. 2017. Cancer immunotherapies targeting the PD-1 signaling pathway. *J. Biomed. Sci*. 24: 26. https://doi.org/10.1186/s12929-017-0329-9

Kamphorst, A.O., A. Wieland, T. Nasti, S. Yang, R. Zhang, D.L. Barber, B.T. Konieczny, C.Z. Daugherty, L. Koenig, K. Yu, et al. 2017. Rescue of exhausted CD8 T cells by PD-1-targeted therapies is CD28-dependent. *Science*. 355:1423–1427. https://doi.org/10.1126/science.aaf0683

Keir, M.E., M.J. Butte, G.J. Freeman, and A.H. Sharpe. 2008. PD-1 and its ligands in tolerance and immunity. *Annu. Rev. Immunol*. 26:677–704. https://doi.org/10.1146/annurev.immunol.26.021607.090331

Lanzavecchia, A., G. Iezzi, and A. Viola. 1999. From TCR engagement to T cell activation: a kinetic view of T cell behavior. *Cell*. 96:1–4. https://doi.org/10.1016/S0092-8674(00)80952-6

Latchman, Y., C. Wood, T. Chernova, Y. Iwai, N. Malenkovich, A. Long, K. Bourque, V. Boussiotis, H. Nishimura, T. Honjo, et al. 2001. PD-L2, a novel B7 homologue, is a second ligand for PD-1 and inhibits T cell activation. *Nat. Immunol*. 2:261–268.

Lenschow, D.J., T.L. Walunas, and J.A. Bluestone. 1996. CD28/B7 system of T cell costimulation. *Annu. Rev. Immunol*. 14:233–258. https://doi.org/10.1146/annurev.immunol.14.1.233

Lo, T.C., L.M. Barnhill, Y. Kim, E.A. Nakae, A.L. Yu, and M.B. Diccianni. 2009. Inactivation of SHIP1 in T-cell acute lymphoblastic leukemia due to mutation and extensive alternative splicing. *Leuk. Res*. 33:1562–1566. https://doi.org/10.1016/j.leukres.2009.04.032

Lorenz, U.. 2009. SHP-1 and SHP-2 in T cells: two phosphatases functioning at many levels. *Immunol. Rev*. 228:342–359. https://doi.org/10.1111/j.1600-065X.2008.00760.x

Mellman, I., G. Coukos, and G. Dranoff. 2011. Cancer immunotherapy comes of age. *Nature*. 480:480–489. https://doi.org/10.1038/nature10673

Meng, X., X. Liu, X. Guo, S. Jiang, T. Chen, Z. Hu, H. Liu, Y. Bai, M. Xue, R. Hu, et al. 2018. FBXO38 mediates PD-1 ubiquitination and regulates anti-tumour immunity of T cells. *Nature*. 564:130–135. https://doi.org/10.1038/s41586-018-0756-0

Mintz, M.A., J.H. Felce, M.Y. Chou, V. Mayya, Y. Xu, J.W. Shui, J. An, Z. Li, A. Marson, T. Okada, et al. 2019. The HVEM-BTLA Axis Restrains T Cell Help to Germinal Center B Cells and Functions as a Cell-Extrinsic Suppressor in Lymphomagenesis. *Immunity*. 51:310–323.e7. https://doi.org/10.1016/j.immuni.2019.05.022

Xu et al.
Comparative analysis of PD-1 and BTLA signaling

Journal of Cell Biology   19 of 20
https://doi.org/10.1083/jcb.201905085

Morel, Y., J.M. Schiano de Colella, J. Harrop, K.C. Deen, S.D. Holmes, T.A. Wattam, S.S. Khandekar, A. Truneh, R.W. Sweet, J.A. Gastaut, et al. 2000. Reciprocal expression of the TNF family receptor herpes virus entry mediator and its ligand LIGHT on activated T cells: LIGHT down-regulates its own receptor. *J. Immunol.* 165:4397–4404. https://doi.org/10.4049/jimmunol.165.8.4397

Nishimura, H., and T. Honjo. 2001. PD-1: an inhibitory immunoreceptor involved in peripheral tolerance. *Trends Immunol.* 22:265–268. https://doi.org/10.1016/S1471-4906(01)01888-9

Nishimura, H., M. Nose, H. Hiai, N. Minato, and T. Honjo. 1999. Development of lupus-like autoimmune diseases by disruption of the PD-1 gene encoding an ITIM motif-carrying immunoreceptor. *Immunity.* 11:141–151. https://doi.org/10.1016/S1074-7613(00)80089-8

Nishimura, H., T. Okazaki, Y. Tanaka, K. Nakatani, M. Hara, A. Matsumori, S. Sasayama, A. Mizoguchi, H. Hiai, N. Minato, et al. 2001. Autoimmune dilated cardiomyopathy in PD-1 receptor-deficient mice. *Science.* 291: 319–322. https://doi.org/10.1126/science.291.5502.319

Okazaki, T., A. Maeda, H. Nishimura, T. Kurosaki, and T. Honjo. 2001. PD-1 immunoreceptor inhibits B cell receptor-mediated signaling by recruiting src homology 2-domain-containing tyrosine phosphatase 2 to phosphotyrosine. *Proc. Natl. Acad. Sci. USA.* 98:13866–13871. https://doi.org/10.1073/pnas.231486598

Pardoll, D.M.. 2012. The blockade of immune checkpoints in cancer immunotherapy. *Nat. Rev. Cancer.* 12:252–264. https://doi.org/10.1038/nrc3239

Pasero, C., and D. Olive. 2013. Interfering with coinhibitory molecules: BTLA/HVEM as new targets to enhance anti-tumor immunity. *Immunol. Lett.* 151:71–75. https://doi.org/10.1016/j.imlet.2013.01.008

Patsoukis, N., L. Li, D. Sari, V. Petkova, and V.A. Boussiotis. 2013. PD-1 increases PTEN phosphatase activity while decreasing PTEN protein stability by inhibiting casein kinase 2. *Mol. Cell. Biol.* 33:3091–3098. https://doi.org/10.1128/MCB.00319-13

Pauken, K.E., and E.J. Wherry. 2015. Overcoming T cell exhaustion in infection and cancer. *Trends Immunol.* 36:265–276. https://doi.org/10.1016/j.it.2015.02.008

Peled, M., A.S. Tocheva, S. Sandigursky, S. Nayak, E.A. Philips, K.E. Nichols, M. Strazza, I. Azoulay-Alfaguter, M. Askenazi, B.G. Neel, et al. 2018. Affinity purification mass spectrometry analysis of PD-1 uncovers SAP as a new checkpoint inhibitor. *Proc. Natl. Acad. Sci. USA.* 115:E468–E477. https://doi.org/10.1073/pnas.1710437115

Powles, T., J.P. Eder, G.D. Fine, F.S. Braiteh, Y. Loriot, C. Cruz, J. Bellmunt, H.A. Burris, D.P. Petrylak, S.L. Teng, et al. 2014. MPDL3280A (anti-PD-L1) treatment leads to clinical activity in metastatic bladder cancer. *Nature.* 515:558–562. https://doi.org/10.1038/nature13904

Rieckmann, J.C., R. Geiger, D. Hornburg, T. Wolf, K. Kveler, D. Jarrossay, F. Sallusto, S.S. Shen-Orr, A. Lanzavecchia, M. Mann, et al. 2017. Social network architecture of human immune cells unveiled by quantitative proteomics. *Nat. Immunol.* 18:583–593. https://doi.org/10.1038/ni.3693

Riley, J.L.. 2009. PD-1 signaling in primary T cells. *Immunol. Rev.* 229:114–125. https://doi.org/10.1111/j.1600-065X.2009.00767.x

Rizvi, N.A., J. Mazières, D. Planchard, T.E. Stinchcombe, G.K. Dy, S.J. Antonia, L. Horn, H. Lena, E. Minenza, B. Mennecier, et al. 2015. Activity and safety of nivolumab, an anti-PD-1 immune checkpoint inhibitor, for patients with advanced, refractory squamous non-small-cell lung cancer (CheckMate 063): a phase 2, single-arm trial. *Lancet Oncol.* 16: 257–265. https://doi.org/10.1016/S1470-2045(15)70054-9

Rota, G., C. Niogret, A.T. Dang, C.R. Barros, N.P. Fonta, F. Alfei, L. Morgado, D. Zehn, W. Birchmeier, E. Vivier, et al. 2018. Shp-2 Is Dispensable for Establishing T Cell Exhaustion and for PD-1 Signaling In Vivo. *Cell Rep.* 23:39–49. https://doi.org/10.1016/j.celrep.2018.03.026

Schildberg, F.A., S.R. Klein, G.J. Freeman, and A.H. Sharpe. 2016. Coinhibitory Pathways in the B7-CD28 Ligand-Receptor Family. *Immunity.* 44: 955–972. https://doi.org/10.1016/j.immuni.2016.05.002

Sedy, J.R., M. Gavrieli, K.G. Potter, M.A. Hurchla, R.C. Lindsley, K. Hildner, S. Scheu, K. Pfeffer, C.F. Ware, T.L. Murphy, et al. 2005. B and T lymphocyte attenuator regulates T cell activation through interaction with herpesvirus entry mediator. *Nat. Immunol.* 6:90–98. https://doi.org/10.1038/ni1144

Sharma, P., and J.P. Allison. 2015. The future of immune checkpoint therapy. *Science.* 348:56–61. https://doi.org/10.1126/science.aaa8172

Sheppard, K.A., L.J. Fitz, J.M. Lee, C. Benander, J.A. George, J. Wooters, Y. Qiu, J.M. Jussif, L.L. Carter, C.R. Wood, et al. 2004. PD-1 inhibits T-cell receptor induced phosphorylation of the ZAP70/CD3zeta signalosome and downstream signaling to PKCtheta. *FEBS Lett.* 574:37–41. https://doi.org/10.1016/j.febslet.2004.07.083

Tatsumi, T., T. Takehara, K. Katayama, K. Mochizuki, M. Yamamoto, T. Kanto, Y. Sasaki, A. Kasahara, and N. Hayashi. 1997. Expression of costimulatory molecules B7-1 (CD80) and B7-2 (CD86) on human hepatocellular carcinoma. *Hepatology.* 25:1108–1114. https://doi.org/10.1002/hep.510250511

Taube, J.M., R.A. Anders, G.D. Young, H. Xu, R. Sharma, T.L. McMiller, S. Chen, A.P. Klein, D.M. Pardoll, S.L. Topalian, et al. 2012. Colocalization of inflammatory response with B7-h1 expression in human melanocytic lesions supports an adaptive resistance mechanism of immune escape. *Sci. Transl. Med.* 4. 127ra37. https://doi.org/10.1126/scitranslmed.3003689

Tinti, M., A.P. Nardozza, E. Ferrari, F. Sacco, S. Corallino, L. Castagnoli, and G. Cesareni. 2012. The 4G10, pY20 and p-TYR-100 antibody specificity: profiling by peptide microarrays. *N. Biotechnol.* 29:571–577. https://doi.org/10.1016/j.nbt.2011.12.001

Topalian, S.L., F.S. Hodi, J.R. Brahmer, S.N. Gettinger, D.C. Smith, D.F. McDermott, J.D. Powderly, R.D. Carvajal, J.A. Sosman, M.B. Atkins, et al. 2012. Safety, activity, and immune correlates of anti-PD-1 antibody in cancer. *N. Engl. J. Med.* 366:2443–2454. https://doi.org/10.1056/NEJMoa1200690

Truitt, K.E., C.M. Hicks, and J.B. Imboden. 1994. Stimulation of CD28 triggers an association between CD28 and phosphatidylinositol 3-kinase in Jurkat T cells. *J. Exp. Med.* 179:1071–1076. https://doi.org/10.1084/jem.179.3.1071

Wang, B., W. Zhang, V. Jankovic, J. Golubov, P. Poon, E.M. Oswald, C. Gurer, J. Wei, I. Ramos, Q. Wu, et al. 2018. Combination cancer immunotherapy targeting PD-1 and GITR can rescue CD8+ T cell dysfunction and maintain memory phenotype. *Sci. Immunol.* 3. eaat7061. https://doi.org/10.1126/sciimmunol.aat7061

Watanabe, N., M. Gavrieli, J.R. Sedy, J. Yang, F. Fallarino, S.K. Loftin, M.A. Hurchla, N. Zimmerman, J. Sim, X. Zang, et al. 2003. BTLA is a lymphocyte inhibitory receptor with similarities to CTLA-4 and PD-1. *Nat. Immunol.* 4:670–679. https://doi.org/10.1038/ni944

Yokosuka, T., M. Takamatsu, W. Kobayashi-Imanishi, A. Hashimoto-Tane, M. Azuma, and T. Saito. 2012. Programmed cell death 1 forms negative costimulatory microclusters that directly inhibit T cell receptor signaling by recruiting phosphatase SHP2. *J. Exp. Med.* 209:1201–1217. https://doi.org/10.1084/jem.20112741

Zhao, Q., Z.L. Huang, M. He, Z. Gao, and D.M. Kuang. 2016. BTLA identifies dysfunctional PD-1-expressing CD4+ T cells in human hepatocellular carcinoma. *OncoImmunology.* 5. e1254855. https://doi.org/10.1080/2162402X.2016.1254855

Zhao, Y., D.L. Harrison, Y. Song, J. Ji, J. Huang, and E. Hui. 2018. Antigen-Presenting Cell-Intrinsic PD-1 Neutralizes PD-L1 in cis to Attenuate PD-1 Signaling in T Cells. *Cell Rep.* 24:379–390.e6. https://doi.org/10.1016/j.celrep.2018.06.054

Supplemental material

A BTLA expression

— Jurkat parental: Isotype
— Jurkat parental: anti-BTLA PE

B CD28 expression

— Jurkat (PD-1WT-mGFP+): Isotype
— Jurkat (PD-1FF-mGFP+): anti-CD28 APC
— Jurkat (PD-1WT-mGFP+): anti-CD28 APC
— Jurkat (BTLAFFFF-mGFP+): anti-CD28 APC
— Jurkat (BTLAWT-mGFP+): anti-CD28 APC

C
mGFP Stds/pmol   IP PD-1/µl   IP BTLA/µl
4.3 2.1 1.1 0.56   10   5   10   5

GFP IB

- 100 kD
- 75 kD
- 35 kD
- 25 kD

[BTLA] in Jurkat cells: 0.59 µM
[PD-1] in Jurkat cells: 2.97 µM

D HVEM/PD-L1 expression

— Raji (HVEM-mRuby+): Isotype
— Raji (PD-L1-mCherry+): Isotype
— Raji (HVEM-mRuby+): anti-HVEM APC
— Raji (PD-L1-mCherry+): anti-PD-L1 APC

Figure S1. **Expression levels of BTLA, CD28, HVEM, and PD-L1 on Jurkat or Raji cells. (A)** Flow cytometry histograms of BTLA surface expression in parental Jurkat cells. **(B)** Flow cytometry histograms of CD28 surface expressions in the indicated types of Jurkat cells. **(C)** Quantification of BTLA-mGFP and PD-1–mGFP in Jurkat (BTLA-mGFP+) and Jurkat (PD-1–mGFP+) cells, respectively. 4×10^6 Jurkat (BTLA-mGFP+) cells or Jurkat (PD-1–mGFP+) cells were lysed on ice using PBS containing 1% NP-40 and protease inhibitors. BTLA-mGFP and PD-1–mGFP were then immunoprecipitated using GFP-Trap and eluted by 50 µl SDS sample buffer. 10 µl and 5 µl of the eluates were loaded to SDS-PAGE together with indicated amounts of purified mGFP protein as standards (Stds). BTLA-mGFP and PD-1–mGFP were then quantified using a standard curve constructed based on the mGFP standards and their concentrations in Jurkat cells calculated by dividing the number of moles by the average volume of a Jurkat cell, assuming a 12-µm diameter for Jurkat cells. **(D)** Red histogram indicates HVEM surface expression in Raji (HVEM-mRuby+) cells. Blue histogram indicates PD-L1 surface expression on Raji (PD-L1–mCherry+) cells. Gray and black histograms show isotype control staining.

A

Amino acid sequences of WT and mutant BTLA intracellular tails:

```
                     226              243              257                        282
BTLAINT (WT):    QNSQVLLSETGIYDNDPDLCFRMQEGSEVYSNPCLEENKPGIVYASLNHSVIGPNSRLARNVKEAPTEYASICVRS
BTLAINT (YFFF):  QNSQVLLSETGIYDNDPDLCFRMQEGSEVFSNPCLEENKPGIVFASLNHSVIGPNSRLARNVKEAPTEFASICVRS
BTLAINT (FYFF):  QNSQVLLSETGIFDNDPDLCFRMQEGSEVYSNPCLEENKPGIVFASLNHSVIGPNSRLARNVKEAPTEFASICVRS
BTLAINT (FFYF):  QNSQVLLSETGIFDNDPDLCFRMQEGSEVFSNPCLEENKPGIVYASLNHSVIGPNSRLARNVKEAPTEFASICVRS
BTLAINT (FFFY):  QNSQVLLSETGIFDNDPDLCFRMQEGSEVFSNPCLEENKPGIVFASLNHSVIGPNSRLARNVKEAPTEYASICVRS
```

B

```
                        ATP    ●  ●  ●  ●
                        Lck    ●  ●  ●  ●
His10-BTLAINT (YFFF)    ●  ○  ○  ○
His10-BTLAINT (FYFF)    ○  ●  ○  ○
His10-BTLAINT (FFYF)    ○  ○  ●  ○
His10-BTLAINT (FFFY)    ○  ○  ○  ●
```

anti-pY IB   - 25 kD
                    - 20 kD
anti-His IB   - 25 kD
                    - 20 kD

Figure S2. **Anti-pY antibody pY20 prefers pY226 and pY243 over pY257 and pY282 of BTLAINT. (A)** Amino acid sequences of WT BTLAINT and single Y mutants used for testing the preference of pY20. **(B)** IBs showing the preferences of pY20 among the four phosphorylatable tyrosine residues within BTLAINT. Similar levels of purified His10-BTLAINT (YFFF), His10-BTLAINT (FYFF), His10-BTLAINT (FFYF), and His10-BTLAINT (FFFY) were loaded as indicated by anti-His IB.
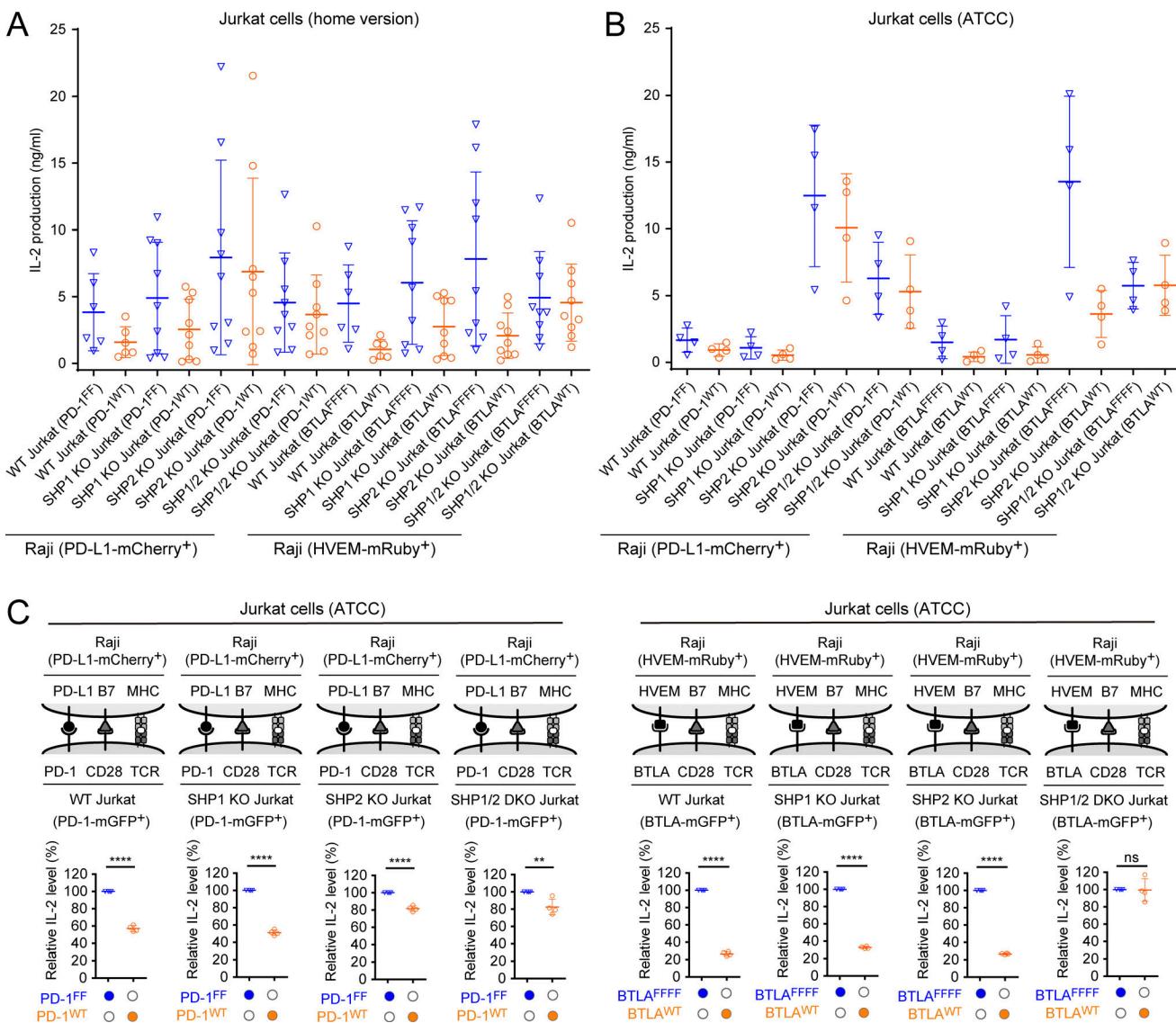
Figure S3. **Effects of PD-1 and BTLA signaling on IL-2 production in WT, SHP1 KO, SHP2 KO, and SHP1/2 DKO Jurkat cells. (A)** Raw IL-2 levels in the medium of the indicated Raji-Jurkat co-cultures. Data are means ± SD from six to nine independent experiments. These are also the raw data for Fig. 6, F–H. **(B)** Raw IL-2 levels in the medium of the indicated Raji-Jurkat co-cultures, using Jurkat clones based upon the Jurkat E6.1 recently obtained from ATCC. Data are means ± SD from four independent experiments. **(C)** Scatter plots showing relative IL-2 levels of the indicated Raji-Jurkat co-cultures. Data are the same as B, except that in each replicate IL-2 levels of Jurkat (PD-1^{WT}–mGFP$^+$) or Jurkat (BTLA^{WT}-mGFP$^+$) were normalized to that of Jurkat (PD-1^{FF}–mGFP$^+$) or to that of Jurkat (BTLA^{FFFF}-mGFP$^+$) under the same SHP background, respectively (see Materials and methods). **, P < 0.01; ****, P < 0.0001; ns, not significant; Student's t test (n = 4).
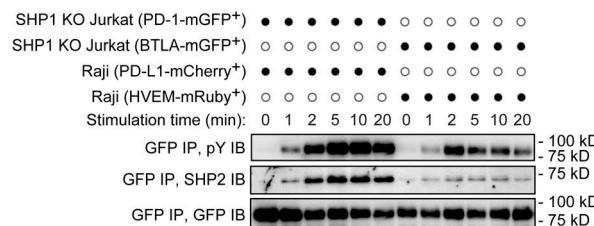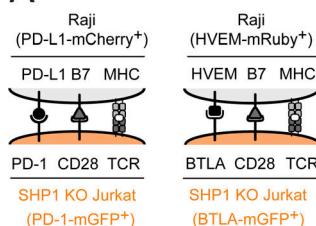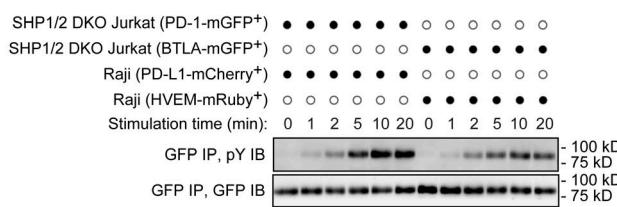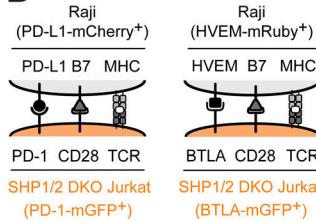
Figure S4. Phosphorylation of PD-1 and BTLA in SHP1 KO or SHP1/2 DKO Jurkat cells. (A) IBs showing the phosphorylation and SHP2 association of PD-1–mGFP or BTLA-mGFP immunoprecipitated from the lysates of the indicated co-cultures, with the stimulation time indicated (see Materials and methods). GFP IB indicates the input of PD-1–mGFP or BTLA-mGFP. **(B)** Same as A, except using SHP1/2 DKO Jurkat cells instead of SHP1 KO Jurkat cells.
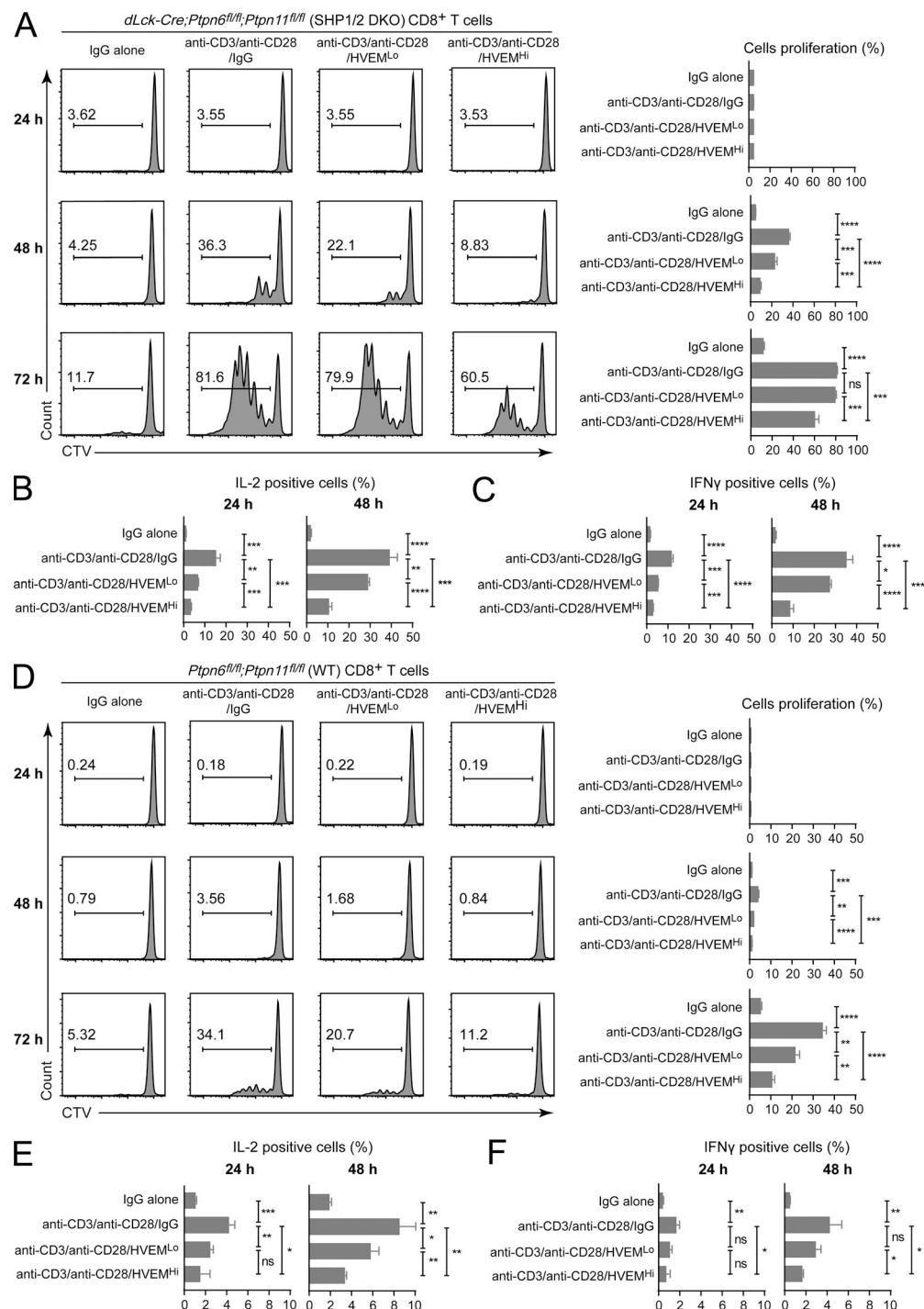
Figure S5. **HVEM inhibits the functions of mouse primary T cells deficient in both SHP1 and SHP2. (A)** SHP1/2 DKO CD8+ T cells freshly isolated from *dLck-Cre;Ptpn6fl/fl;Ptpn11fl/fl* mice were stained with CTV dye and stimulated with protein G Dynabeads precoated with IgG alone, anti-CD3/anti-CD28/IgG, anti-CD3/anti-CD28/HVEM-Fc^low, or anti-CD3/anti-CD28/HVEM-Fc^high, respectively (see Materials and methods). Flow cytometry diagrams on the left show the degrees of CTV dilution as a consequence of cell proliferation at 24, 48, and 72 h under the indicated stimulation conditions. The number denotes percentage of proliferating cells. Bar graphs on the right summarize the percentage of proliferating cells in three technical replicates. **(B)** Percentage of IL-2–positive cells 24 and 48 h after the indicated stimulation, measured by flow cytometry. **(C)** Percentage of IFN-γ+ cells 24 and 48 h after the indicated stimulation, measured by flow cytometry. **(D–F)** Same as A–C, except using WT CD8+ T cells freshly isolated from *Ptpn6fl/fl;Ptpn11fl/fl* mice. Data in this figure are presented as means ± SD. *, P < 0.05; **, P < 0.01; ***, P < 0.001; ****, P < 0.0001; ns, not significant; Student's *t* test (*n* = 3).

Xu et al.
Comparative analysis of PD-1 and BTLA signaling

Journal of Cell Biology   S4
https://doi.org/10.1083/jcb.201905085

Video 1.   **Time-lapse TIRF imaging of PLB-interacting Jurkat cells showing that PD-1 microclusters recruited SHP2 but not SHP1.** Same as Fig. 3 C except showing live movies instead of snapshot images. Movie duration: 16.5 min. Frame interval: 10 s. Scale bars: 5 µm.

Table S1 is provided online and shows the percentage of IL-2 inhibition mediated by PD-1 or BTLA in various PTPase backgrounds.